

# Magnetic anisotropy and related matters. Studied by neutron diffraction

**Aarosin Hansen, P.**

*Publication date:*
1977

*Document Version*
Publisher's PDF, also known as Version of record

Risø Report No. 360

Risø Report No. 360

Risø National Laboratory

# Magnetic Anisotropy and Related Matters Studied by Neutron Diffraction

*by* Peter Aarosiin Hansen

July 1977

*Sales distributors:* Jul. Gjellerup, Sølvgade 87, DK-1307 Copenhagen K, Denmark

*Available on exchange from:* Risø Library, Risø National Laboratory, DK-4000 Roskilde, Denmark

UDC 546.65 : 538.22 : 548.78

Risø Report No. 360

# MAGNETIC ANISOTROPY AND RELATED MATTERS STUDIED BY NEUTRON DIFFRACTION

Peter Aarosiin Hansen

Physics Department

Risø National Laboratory, Denmark

July 1977

Risø Repro 1977

ISBN 87-550-0485-7

**ABSTRACT**

Single crystals of Tb-Tm alloys, Nd and MnSi were investigated by neutron diffractometry. Four Tb-Tm alloys with a Tm content of 12%, 40%, 55% and 65% were investigated in the temperature range of 4.2-300 K.

All these alloys order magnetically to a basal plane spiral below the Néel temperature. Below the Curie temperature the magnetic ordering of the Tb-12% Tm alloy is ferromagnetic with the moments in the basal plane, while the other alloys have a ferromagnetic component along the c-axis and a spiral component in the basal plane below $T_C$. The Tb-55% Tm and the Tb-65% Tm alloys have an intermediate mixed phase, where the c-axis component is modulated along the c-axis (CAM-structure). In contrast to all other heavy rare earth alloys studied so far, these neutron diffraction studies show unambiguously that Tb-Tm alloys have an inhomogeneous phase, where the spins associated with the Tb-ions lie in the basal plane, while the spins associated with the Tm-ions order along the c-axis.

The magnetic structure of Nd was investigated between 4.2 K and the ordering temperature 20 K. It is shown that the magnetic structure can be understood with the assumption of single ion anisotropy and that the measured magnetic intensities are not in agreement with the magnetic model proposed by Moon et al. (1964). The critical exponent $\beta$ is in agreement with the $\varepsilon$-expansion. MnSi is shown to be an example of a magnetic material with magnetism of nearly itinerant character. The magnetic structure is a spiral structure below the ordering temperature (26.7 K). The screw axis is the (111) direction and the modulation vector is very short (0.036 $Å^{-1}$). In a magnetic field the structure transform into a cone structure at 1 kGauss and above 6 kGauss it is ferromagnetic.

---

This report is submitted to the Technical University of Denmark in partial fulfilment of the requirements for obtaining the lic.techn. (Ph.D.) degree.

CONTENTS

Page

List of symbols ..... 7

Introduction ..... 11
1. Magnetism of the Rare Earth Elements ..... 13
   1.1. Exchange Interaction ..... 14
   1.2. Crystal Field Interaction ..... 17
   1.3. Magnetostriction ..... 21

2. Magnetic Interactions in an Alloy of Rare Earth Metals 22
   2.1. Molecular Field Theory for an Alloy System ..... 22
   2.2. Two-ion Anisotropy ..... 27

3. Experimental Method ..... 28
   3.1. Sample Preparation ..... 28
   3.2. Neutron Diffraction Techniques ..... 32
   3.3. Description of the Diffractometer ..... 38
   3.4. Experimental Problems ..... 40

4. Tb-Tm Alloy System ..... 42
   4.1. Introduction ..... 42
   4.2. Magnetic Properties and Structures of Pure Tb and Pure Tm ..... 42
   4.3. Description of the Experimental Results ..... 45
   4.4. Discussion of the Experimental Results ..... 55
   4.5. Conclusion ..... 58

5. Magnetic Structure and Critical Behaviour of Nd ..... 59
   5.1. Introduction ..... 59
   5.2. Magnetic Structure of Nd ..... 60
   5.3. Critical Behaviour of Nd ..... 65

6. Magnetic Structure of MnSi ..... 69
   6.1. Introduction ..... 69
   6.2. Experimental Results ..... 71
   6.3. Conclusions ..... 76

Acknowledgements ..... 76
References ..... 77

## LIST OF SYMBOLS

| | |
|---|---|
| $a,b,c,$ | lattice constants |
| $a_o$ | Bohr radius |
| $B_j^i$ | crystal field constants |
| $B_\ell(r)$ | Bessel function |
| $B_j$ | Brillouin function |
| $d$ | distance between the planes of the lattice |
| $\underline{d}_i$ | atomic positions within the unit cell |
| $\frac{d\sigma}{d\Omega}$ | differential scattering cross section |
| $e$ | charge of the electron |
| $e^{-2W}$ | Debye-Waller factor |
| $f(\underline{\kappa})$ | magnetic form factor |
| $F(\underline{\tau})$ | geometrical structure factor |
| $g(\underline{r})$ | r-dependence of the wave function |
| $g$ | Landé factor |
| $\hbar$ | Planck constant divided by $2\pi$ |
| $H_{ex}$ | exchange Hamiltonian |
| $H_{cr}$ | crystal field Hamiltonian |
| $<j_\ell>$ | see eq. 3.2.19 |
| $\underline{J}$ | total angular momentum |
| $\mathcal{J}$ | exchange constant |
| $k_B$ | Boltzmann's constant |
| $\underline{k}$ | wave vector of the neutron |
| $\underline{L}$ | orbital momentum |
| $m$ | mass of the neutron |
| $M$ | mass of the atom |
| $\underline{M}$ | total magnetic moment |
| $N$ | number of atoms in a crystal |

| | |
|---|---|
| $O_\ell^m$ | Stevens operators |
| $p$ | $= \frac{1}{2}\gamma r_o = 0.2695 \cdot 10^{-12}$ cm |
| $\underline{q}$ | wave vector |
| $\underline{Q}$ | modulation vector |
| $\underline{R}$ | lattice vector |
| $r_o$ | classical electron radius |
| $\underline{s}$ | spin moment |
| $T$ | absolute temperature |
| $T_N$ | Néel temperature |
| $T_c$ | Curie temperature |
| $u_\ell(\underline{r})$ | spin density |
| $V$ | volume of the unit cell |
| $Y_i^j$ | spherical harmonics |
| $z$ | number of electrons |
| $Z$ | partition function |
| $\beta$ | $1/k_B T$ |
| $\bar{\gamma}$ | gyromagnetic moment of the neutron |
| $\delta(\underline{r})$ | Dirac $\delta$-function |
| $\varepsilon$ | energy of the electron |
| $\varepsilon_f$ | Fermi energy |
| $\hat{\kappa}$ | unit vector along the scattering vector |
| $\underline{\kappa}$ | scattering vector |
| $\lambda$ | wave length |
| $\chi$ | susceptibility |

$\underline{\mu}_n$ magnetic moment of the ion at site n

$\phi$ angle between the c-axis and the scattering vector

$\underline{\sigma}_n$ spin of the neutron

$\underline{\tau}$ reciprocal lattice vector

$2\theta$ scattering angle

$\theta_D$ Debye temperature

# INTRODUCTION

Nearly all magnetic materials are magnetically anisotropic. In order to investigate the origin of this anisotropy, we studied alloys of magnetic ions which have totally different magnetic anisotropy.

We chose to investigate Tb-Tm alloys because both Tb and Tm are highly magnetically anisotropic; they have an identical crystallographic structure, their ionic charges are equal, and their ionic radii are nearly equal in magnitude. As concluded in sec. 4.3, the magnetic anisotropy of the individual ions is the same in the alloys and in the pure elements. We therefore conclude that the magnetic anisotropy is not caused by a spin-spin interaction (exchange-interaction) but by the crystalline field (see sec. 1.2).

As discussed in chapter 2, our magnetic model for the Tb-Tm alloys mainly consists of two interactions, namely isotropic exchange and crystal field interaction. The isotropic exchange interaction can be split into three terms, which describe the interactions between the Tb-Tb ions, the Tm-Tm ions and the Tb-Tm ions. It is very interesting to use the same model on a system consisting of only one type of ion, but where there are two different sites with different crystal fields. Pure Nd has this property (see sec. 5.2) and although we were unable to determine the magnetic structure in detail, the magnetic model mentioned above seems to be valid in this case (see chap. 5).

It is assumed above that we are dealing with localized magnetic moments. This is an extremely good approximation for a rare earth (see sec. 1.1), but in the case of 3d-metals we deal with magnetic systems where some of the magnetism is bound to the conduction electrons. Such systems where the magnetism has a partly itinerant character are very difficult to handle theoretically, but in the limit where the magnetism is totally itinerant it becomes fairly easy to treat by band theory. MnSi, which is discussed in sec. 6, seems an example of this type.

The most striking feature of magnetic systems is, of course, the phase transitions. The great variety of phase transitions in magnetic systems, and fair understanding of the basic theory of these systems, makes them very attractive to study in

connection with phase transitions. Very recently there has been a break-through in the theory of phase transitions, and numerous critical exponents have been calculated using the Wilson (1974) theory. We measured the critical exponent of Nd, and it is in agreement with that calculated by Mukamel et al. (1976). If the magnetism of MnSi is of totally itinerant character, we would expect the transition from the ordered to the disordered phase to be of first order. As discussed in sec. 6.2, this seems to be the case.

Before proceeding to the experimental results (Tb-Tm in chap. 4, Nd in chap. 5 and MnSi in chap. 6), some of the basic theory for the magnetism of the rare earths is discussed in chaps. 1 and 2. Chapter 3 deals with the experimental method.

# 1. THE MAGNETISM OF THE RARE EARTH ELEMENTS

The magnetism of the rare earth metals results from the unfilled 4f-electron shell. This deep-lying shell is shielded by 5p and 5s electrons, and the magnetic ions in a solid can therefore be treated as nearly free ions. This fact much simplifies the theoretical treatment. The magnetic moments are well localized and the ions are characterized by the total angular momentum $\underline{J}$. The other $\underline{J}$-levels are separated several hundreds of degrees from the ground level due to the spin-orbit coupling and can be neglected in connection with the magnetic interaction. The total orbital momentum $\underline{L}$ and the total spin momentum $\underline{S}$ are determined by Hund's rules. There is no direct exhange interaction between the ions because the 4f wave functions do not overlap, but the ions interact via the conduction electrons (indirect exchange, see sec. 1.1). Because the 4f-electron wave functions are non-spherical (except for Gd), there is an interaction with the electric field originating from the charges of the surrounding ions (sec. 1.2 and 1.3). It is valuable to compare this picture of the magnetism in the rare earths with that of the iron-group metals. The 3d-electrons, which are responsible for the magnetism of the iron-group metals, are not so well shielded by the outer electrons. The magnetic moments are not localized because the 3d-electrons are free to move in the solid. The spin-orbit coupling breaks down because of crystal field effects. The magnetism of the iron-group metals has to be treated by band theory, which is much more complicated than the theory for the magnetism of the rare earths. The possibility of a rather simple theoretical treatment of the rare earth metals is responsible for the great activity in this field in the last decades.

The experimental results to be described in sections 4 and 5 are derived from studying magnetic structures. The magnetic structures of the heavy rare earths are well known. As seen in fig. 1.1.1 (Koehler 1972), there is a wide variety of magnetic ordering depending on the heavy rare earth ion and the temperature. Nd, which belongs to the light rare earths, has an even more complicated magnetic structure and as explained in sec. 5.2, we do not yet know the details of this structure. In the following sections a brief discussion will be given of the

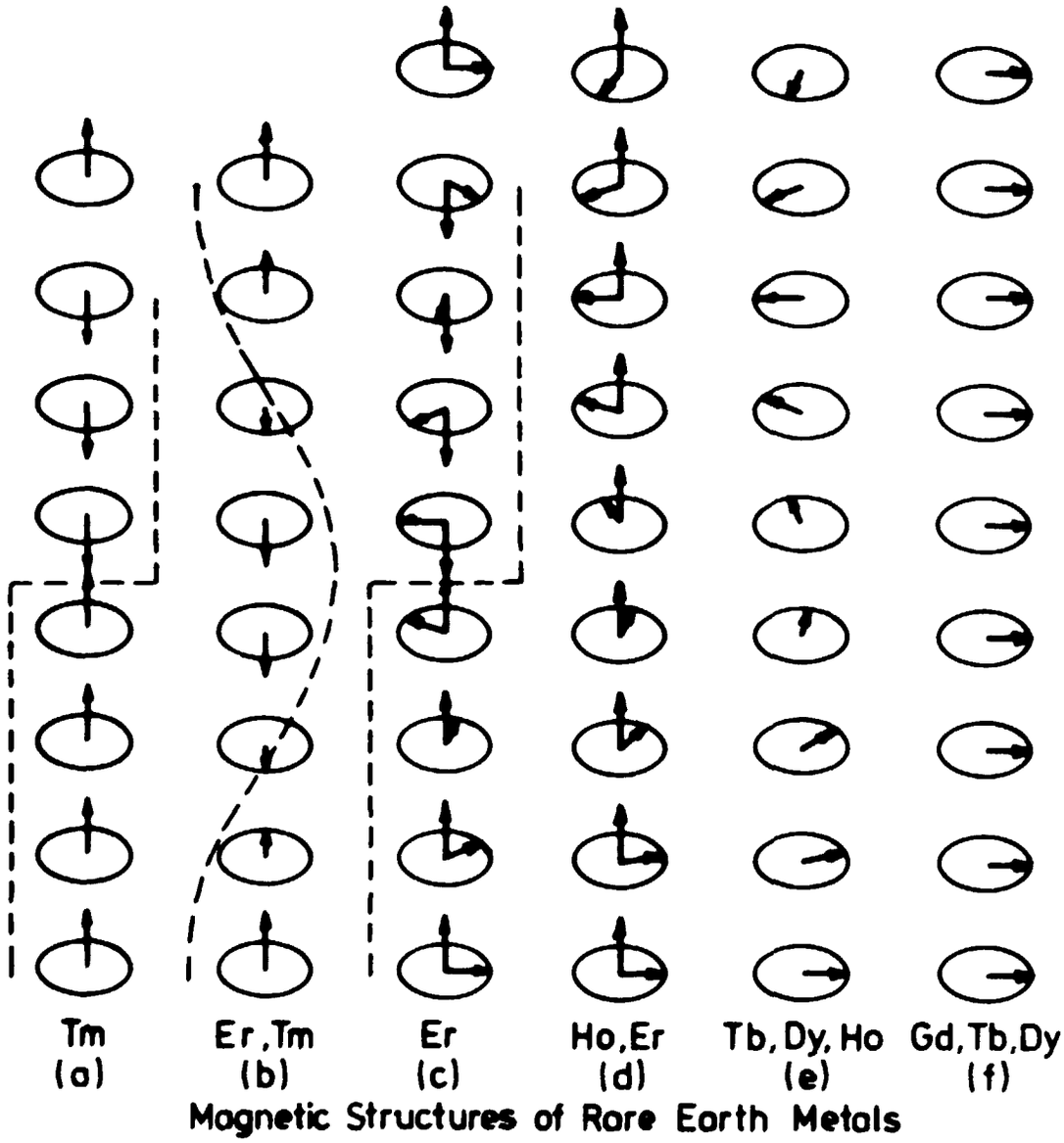


Fig. 1.1.1. The magnetic structures of the heavy rare earths. The c-axis of the hexagonal lattice is vertical. The magnetic moments are ferromagnetically ordered within each hexagonal layer, and the figure shows how the magnetic moments change from one hexagonal layer to the next (from Koehler 1972).

magnetic interactions that are responsible for the observed magnetic structures. These magnetic interactions are most easily described in three sections: the exchange interaction, the crystal field interaction and magnetostriction.

## 1.1. Exchange interaction

Because of the lack of overlap between the 4f-electron wave function, there is no direct exchange interaction. The exchange

interaction takes place indirectly via the conduction electrons. This type of interaction (the RKKY interaction) has been investigated by Ruderman and Kittel (1954), Kasuya (1956) and Yosida (1957) and has the form

$$H_{ex} = - \sum_{ij} \tilde{J}(\underline{R}_i - \underline{R}_j)\underline{S}_i \cdot \underline{S}_j \qquad (1.1.1)$$

where $\underline{S}_i$ is the moment of atom i localized at $\underline{R}_i$. $\tilde{J}(\underline{R}_i - \underline{R}_j)$ is an oscillating function of long range, which depends on the distance between the ions. The energy splitting between the J-levels is so large that the total spin $\underline{S}$ can be projected onto the total angular momentum

$$\underline{S} = (g - 1)\underline{J} \qquad (1.1.2)$$

and thereby

$$H_{ex} = - \sum_{ij} (g_i - 1)\ (g_j - 1)\tilde{J}(\underline{R}_i - \underline{R}_j)\underline{J}_i \cdot \underline{J}_j. \qquad (1.1.3)$$

If we Fourier transform the exchange constant

$$\tilde{J}(\underline{q}) = \sum_i \tilde{J}(\underline{R}_i)\exp(-i\underline{q} \cdot \underline{R}_i) \qquad (1.1.4)$$

and the total spins

$$\underline{S}_{\underline{q}} = \sum_i \underline{S}_i \exp(-i\underline{q} \cdot \underline{R}_i), \qquad (1.1.5)$$

we get

$$H_{ex} = - \sum_{\underline{q}} \tilde{J}(\underline{q})\underline{S}_{\underline{q}} \cdot \underline{S}_{-\underline{q}} \ . \qquad (1.1.6)$$

By a rather simple argument, derived by Nagamiya (1967), it is possible to see that this Hamiltonian can give rise to oscillating magnetic structures such as those shown in fig. 1.1.1. We neglect the anisotropy energy for the moment and treat the spins as classical spins. For simplification, we look for a minimum in the exchange energy, even though we should minimize the free energy. We have the condition that $S_n^2 = \text{const.} = S^2$

for all n. Instead of this condition, we can impose the milder condition that

$$\sum_i \underline{S}_i^2 = \text{const.}, \qquad \text{or} \sum_q \underline{S}_q \cdot \underline{S}_{-q} = \text{const.} \tag{1.1.7}$$

Under this condition, we find that $H_{ex}$ is minimized when $\tilde{J}(\underline{q})$ has its largest value $\tilde{J}(\underline{Q})$. The minimum value of $H_{ex}$ is given by

$$H_{ex} = -\tilde{J}(\underline{Q})\ (\underline{S}_{\underline{Q}} \cdot \underline{S}_{-\underline{Q}} + \underline{S}_{-\underline{Q}} \cdot \underline{S}_{\underline{Q}}). \tag{1.1.8}$$

From (1.1.5) we find that

$$\underline{S}_n = N^{-1}[\underline{S}_{\underline{Q}} \exp(i\underline{Q} \cdot \underline{R}_n) + \underline{S}_{-\underline{Q}} \exp(-i\underline{Q} \cdot \underline{R}_n)] \tag{1.1.9}$$

or

$$\begin{aligned} S_{nx} &= A \cos(\underline{Q} \cdot \underline{R}_n + \alpha) \\ S_{ny} &= B \cos(\underline{Q} \cdot \underline{R}_n + \beta) \\ S_{nz} &= C \cos(\underline{Q} \cdot \underline{R}_n + \gamma) \end{aligned} \tag{1.1.10}$$

where A, B, C, and $\alpha$, $\beta$, $\gamma$ are constants. By a suitable choice of these constants, this equation can be used to describe some of the magnetic structures shown in fig. 1.1.1.

In the free electron model it is possible to calculate the Fourier transform of the exchange constants (Rudermann and Kittel 1954)

$$\tilde{J}(\underline{q}) = \frac{3z\,w^2}{16\,\varepsilon_f}\left(1 + \frac{1-x^2}{2x}\ln\left|\frac{1+x}{1-x}\right|\right) \tag{1.1.11}$$

where $x = \frac{q}{2k_f}$

z is the number of conduction electrons, $k_f$ is the length of the wavevector at the Fermi level $\varepsilon_f$, and w is the exchange integral for the interaction between the 4f-electron and the conduction electron. By Fourier inverting, we get

$$\tilde{J}(\underline{R}) = \frac{3zw^2}{2\varepsilon_f}\,(y \cos y - \sin y)/y^4 \tag{1.1.12}$$

where $y = 2k_f R$. R is the distance in direct space. This equation shows the oscillating nature of the exchange interaction and that is is of long range.

For a general electron band structure, $\tilde{J}(\underline{q})$ is given by an expression of the form (Roth et al. 1966)

$$\tilde{J}(\underline{q}) = \sum_{n,n',\underline{k}} \frac{I_{nn'}(\underline{k},\underline{k}+\underline{q}+\underline{\tau})\ f(\varepsilon_n(\underline{k}))\ [1-f(\varepsilon_{n'}(\underline{k}+\underline{q}+\underline{\tau}))]}{\varepsilon_{n'}(\underline{k}+\underline{q}+\underline{\tau}) - \varepsilon_n(\underline{k})} \tag{1.1.13}$$

where $\varepsilon_n(\underline{k})$ is the energy of a Bloch state of wavevector $\underline{k}$ in band n, $I_{nn'}(\underline{k},\underline{k}+\underline{q}+\underline{\tau})$ is a slowly varying exchange integral and $\underline{\tau}$ is a reciprocal lattice vector chosen so that $\underline{q}$ lies in the first Brillouin zone. $f(\varepsilon)$ is the Fermi function

$$f(\varepsilon) = 1/[\exp((\varepsilon-\varepsilon_f)/k_BT) + 1]. \tag{1.1.14}$$

A number of sources can be responsible for an anisotropic exchange interaction. The most important has been treated by Kaplan (1961) and has the form of a dipole-dipole interaction

$$H_{ex,an} = - \sum_{i\neq j} k_{ij}\, J_{zi} \cdot J_{zj} \tag{1.1.15}$$

where $J_{zi}$ is the z-component of $\underline{J}_i$. Kaplan and Lyons (1961) estimated this interaction to be of the order of 10% of the isotropic exchange interaction.

## 1.2. Crystal field interactions

The crystal field interaction results from the electric field from the surrounding ions. The interaction is most easily treated in the point charge model. Although this model is too crude to give quantitative agreement with experiments, it is believed to give the right form of the interaction. In the model it is assumed that the charges of the surrounding ions are located at the lattice points. These charges will be screened by the outer electrons, and we can neglect ions other than the nearest neighbours. With these assumptions, the energy of an electron positioned at $\underline{r}$ will be

$$V(\underline{r}) = - \sum_j \frac{ze^2}{|\underline{R}_j - \underline{r}|} \tag{1.2.1}$$

where the summation is over the nearest neighbours at $\underline{R}_j$ with the effective charge ze. Equation 1.2.1 may be expanded in

spherical harmonics (Kasuya 1966). For the hcp structure

$$V(\underline{r}) = V_2^0 r^2 Y_2^0(\theta,\phi) + V_4^0 r^4 Y_4^0(\theta,\phi) + V_6^0 r^6 Y_6^0(\theta,\phi) + V_6^6 r^6 [Y_6^6(\theta,\phi) + Y_6^{-6}(\theta,\phi)] \quad (1.2.2)$$

plus higher order terms.

The crystal field Hamiltonian per ion is given by

$$H_{cf} = \sum_i V(\underline{r}_i) \quad (1.2.3)$$

where the summation is over all 4f-electrons. We can determine the crystal field levels by calculating the matrix elements of this operator between Slater determinants consisting of 4f one-electron wave functions. Because the spherical harmonics are orthogonal, we can neglect terms of order higher than 6 in the crystal field Hamiltonian.

An easier way to calculate the crystal field levels is to rewrite $H_{cf}$ in terms of $J_x$, $J_y$, and $J_z$. This can be done by use of the Wigner-Eckart theorem (see e.g. Slichter (1963)) because the ions are characterized by a single J-level due to the strong spin-orbit coupling. This theorem states that within each J-level there is proportionality between matrix elements of the irreducible tensor operator $T_L^M(x_i,y_i,z_i)$ and an equivalent operator as determined by exchanging x, y, and z in the symmetric form of $T_L^M(x,y,z)$ by $J_x$, $J_y$, $J_z$, keeping in mind that $J_x$, $J_y$ and $J_z$ do not commute. The constants of proportionality depend only on the degree of L and can be determined once and for all by calculating a single matrix element by direct integration.

The functions $r^n Y_L^m$ are irreducible tensor operators and $H_{cf}$ can be written in the form

$$H_{cf} = B_2^0 O_2^0(\underline{J}) + B_4^0 O_4^0(\underline{J}) + B_6^0 O_6^0(\underline{J}) + B_6^6 [O_6^6(\underline{J}) + O_6^{-6}(\underline{J})] \quad (1.2.4)$$

where

$$B_2^0 = V_2^0 \alpha \langle r^2 \rangle, \quad B_4^0 = V_4^0 \beta \langle r^4 \rangle,$$

$$B_6^0 = V_6^0 \gamma \langle r^6 \rangle \quad \text{and} \quad B_6^6 = V_6^6 \gamma \langle r^6 \rangle.$$

We have used the common notation for the Stevens factor $\alpha, \beta$ and $\gamma$ (Stevens 1952), which are the constants of proportionality between the matrix elements of the operator $Y_L^m(x,y,z)$ and the matrix elements of the Stevens operator $O_l^m(J_x, J_y, J_z)$. These operators are given by

$$O_2^0 = 3 J_z^2 - J(J+1)$$

$$O_4^0 = 35 J_z^4 - (30J(J+1) - 25) J_z^2 + 3J^2(J+1)^2 - 6J(J+1)$$

$$O_6^0 = 231 J_z^6 - (315J(J+1) - 735) J_z^4 +$$

$$(105J^2(J+1)^2 - 525J(J+1) + 294) J_z^2 -$$

$$5J^3(J+1)^3 + 40J^2(J+1)^2 - 60J(J+1)$$

$$O_6^6 = \tfrac{1}{2}[(J^+)^6 + (J^-)^6].$$

The mean values $\langle r^n \rangle$ are the $r^n$ operators averaged over the radial part of 4f wave functions ($f_{4f}(r)$)

$$\langle r^n \rangle = \int [f_{4f}(r)]^2 r^n r^2 dr. \qquad (1.2.6)$$

These values have been calculated in the Hartree-Fock approximation by Freeman and Watson (1962).

In the point charge model the parameters $V_n^m$ can easily be calculated (Touborg 1970). For the hcp-structure, one finds

that

$$V_2^o = -\frac{ze^2}{a^3}(1.035(1.633 - \frac{c}{a}))$$

$$V_4^o = -\frac{ze^2}{a^5}(0.1127 - 0.752(1.633 - \frac{c}{a}))$$

$$V_6^o = +\frac{ze^2}{a^7}(0.260 + 0.369(1.633 - \frac{c}{a}))$$

$$V_6^6 = -\frac{ze^2}{a^7}(1.26 - 0.409\ (1.633 - \frac{c}{a}))$$

As seen, $V_n^m$ only depends on the lattice parameters and the charge of the surrounding ion. Notice that $V_2^o$ is 0 for an ideal c/a ratio.

In table 1.2.1 are shown the parameters for Tb and Tm that enable us to calculate crystal field levels in the point charge

Table 1.2.1

| | Tb | Tm |
|---|---|---|
| $\alpha \cdot 10^2$ | - 1.01 | 1.01 |
| $\beta \cdot 10^4$ | 1.224 | - 1.224 |
| $\gamma \cdot 10^6$ | - 1.12 | 1.12 |
| $V_2^o(10^{-6}eV) \times a_o^2$ | - 0.802 | - 1.059 |
| $V_4^o(10^{-12}eV) \times a_o^4$ | - 0.244 | - 0.237 |
| $V_6^o(10^{-16}eV) \times a_o^6$ | 0.020 | 0.023 |
| $V_6^6(10^{-16}eV) \times a_o^6$ | - 0.888 | - 1.002 |
| $\frac{1}{a_o^2}\langle r^2 \rangle$ | 0.756 | 0.640 |
| $\frac{1}{a_o^4}\langle r^4 \rangle$ | 1.42 | 1.043 |
| $\frac{1}{a_o^6}\langle r^6 \rangle$ | 5.69 | 3.541 |
| $B_2^o(10^{-3}eV)$ | 0.092 | - 0.103 |
| $B_4^o(10^{-6}eV)$ | -0.095 | 0.068 |
| $B_6^o(10^{-9}eV)$ | -0.043 | 0.021 |
| $B_6^6(10^{-9}eV)$ | 1.91 | -0.89 |

model. If we neglect terms higher than $B_2^o$, the crystal field favours an ordering of the Tb moments in the basal plane. Similarly, $B_2^o$ favours an ordering of the Tm moments along the c-axis, in good agreement with the experimental observations.

Although the point charge model is not in quantitative agreement with the experiments, it is believed to give the correct form of the crystal field Hamiltonian. The parameters $B_2^o$, $B_4^o$, and $B_6^o$ are then to be determined from experiments. As shown by Touborg (1977), $B_4^o/\beta$ and $B_6^o/\gamma$ are universal parameters while $B_2^o/\alpha$ depends on the c/a ratio and the rare earth ion.

## 1.3. Magnetostriction

The magnetic moments will couple to the elastic strains of the crystal through the crystal field interaction. The lattice will deform in order to minimize this magnetoelastic energy together with pure elastic energy. This magnetostriction can be treated as an anisotropic energy of the same form as the crystal field anisotropy, because it will tend to align the moments in a certain direction. The magnitude of this interaction is strongly temperature-dependent, but it is small compared to the crystal field interaction at the transition temperature from ordered to disordered phase. At lower temperatures, magnetostriction plays a more important role and it has been shown that it may be the driving force for the transition from a spiral to a ferromagnetic structure that appears in certain rare earths (Cooper 1972).

Unfortunately, it is very difficult to set up an explicit expression for the magnetostriction, but it is perhaps possible to get valuable information about this interaction by studying phase diagrams like the Tb-Tm phase diagram (see chap. 4).

# 2. MAGNETIC INTERACTIONS IN AN ALLOY OF THE RARE EARTH METALS

In this chapter we will discuss the theoretical treatment of an alloy system of two rare earth metals. The theory will be used to explain the experimental results from the Tb-Tm alloy system, but as discussed in sec. 5 it may also apply to Nd. The theory is chiefly that of Lindgård (1976a). The effect of a possible two-ion anisotropy on the model will be discussed in sec. 2.2.

## 2.1. Molecular field theory for an alloy system

From equation 1.1.3, the exchange interaction between an ion and the surrounding ions is given as

$$H_{ex,i} = \sum_j \tilde{J}_{ji}\, \underline{J}_i \cdot \underline{J}_j \approx \underline{J}_i \cdot \sum_j \tilde{J}_{ji} \langle \underline{J}_j \rangle, \tag{2.1.1}$$

where we have approximated $\underline{J}_j$ by its mean value $\langle \underline{J}_j \rangle$. This is called the molecular field approximation and

$$\underline{M}_i = \sum_j \tilde{J}_{ij} \langle \underline{J}_j \rangle \tag{2.1.2}$$

is the molecular field, because it acts just as a magnetic field on $\underline{J}_i$. By use of eq. 1.1.6, we can write the molecular field in the form

$$\underline{M}_i(\underline{Q}) = \tilde{J}(\underline{Q}) \langle \underline{J}_{\underline{Q}} \rangle. \tag{2.1.3}$$

In the following we drop the indices i and $\underline{Q}$ in order to simplify the notation. In an alloy with two types of ion we have the molecular fields

$$\begin{aligned} \underline{M}_1 &= C_1\, \tilde{J}^{11} \langle \underline{J}_1 \rangle + C_2\, \tilde{J}^{12} \langle \underline{J}_2 \rangle \\ \underline{M}_2 &= C_1\, \tilde{J}^{12} \langle \underline{J}_1 \rangle + C_2\, \tilde{J}^{22} \langle \underline{J}_2 \rangle \end{aligned} \tag{2.1.4}$$

where $C_1$ and $C_2$ are the concentrations and $\tilde{J}^{11}$ and $\tilde{J}^{22}$ are given by the interaction between ions of the same kind, while $\tilde{J}^{12}$ gives the interaction between the two types of ion. Let us for simplicity assume that all the magnetic moments order in the

same direction. Near the ordering temperature, the moments are proportional to the molecular field. The constants of proportionality are the paramagnetic susceptibilities $\chi_1^o$ and $\chi_2^o$. This gives

$$\begin{aligned} \underline{M}_1 &= \frac{1}{\chi_1^o} \langle \underline{J}_1 \rangle = C_1 \tilde{J}^{11} \langle \underline{J}_1 \rangle + C_2 \tilde{J}^{12} \langle \underline{J}_2 \rangle \\ \underline{M}_2 &= \frac{1}{\chi_2^o} \langle \underline{J}_2 \rangle = C_1 \tilde{J}^{12} \langle \underline{J}_1 \rangle + C_2 \tilde{J}^{22} \langle \underline{J}_2 \rangle \end{aligned} \tag{2.1.5}$$

These equations only have solutions different from the trivial one when the determinant is 0. This gives the condition that

$$\frac{1}{\chi_1} \frac{1}{\chi_2} = \left(\frac{1}{\chi_1^o} - C_1 \tilde{J}^{11}\right) \left(\frac{1}{\chi_2^o} - C_2 \tilde{J}^{22}\right) = C_1 C_2 (\tilde{J}^{12})^2 \tag{2.1.6}$$

where $\chi_1$ and $\chi_2$ are enhanced susceptibilities. This is the condition for magnetic ordering of the alloy. For the pure systems the condition is that the enhanced susceptibility goes to zero. Although equation 2.1.6 gives the right condition for ordering of the system, as we shall see below by a more rigorous calculation, we cannot calculate the elemental moments from this equation. To make a more rigorous calculation, we allow $\underline{J}_1$ and $\underline{J}_2$ to fluctuate around their mean values $\langle \underline{J}_1 \rangle$ and $\langle \underline{J}_2 \rangle$, and look for a minimum in the free energy with respect to these fluctuations. In the following we only consider the case where $\langle \underline{J}_1 \rangle$ and $\langle \underline{J}_2 \rangle$ are parallel for simplicity. We write the molecular fields in the form

$$\begin{aligned} M_1 &= C_1 \tilde{J}^{11} (\langle J_1 \rangle + S_1) + C_2 \tilde{J}^{12} (\langle J_2 \rangle + S_2) \\ M_2 &= C_1 \tilde{J}^{12} (\langle J_1 \rangle + S_1) + C_2 \tilde{J}^{22} (\langle J_2 \rangle + S_2) \end{aligned} \tag{2.1.7}$$

where $S_1$ and $S_2$ are variational parameters to be set equal to zero in the final results. Neglecting two-ion anisotropy, we can write the Hamiltonian for the system in terms of the two single-ion Hamiltonians

$$\begin{aligned} \tilde{H}_1 &= - M_1 \cdot J_1 + V_{c1} \\ \tilde{H}_2 &= - M_2 \cdot J_2 + V_{c2} \end{aligned} \tag{2.1.8}$$

where $V_{c1}$ are the crystal fields. The total free energy $F(S_1, S_2)$ is then given by

$$F = - C_1 \frac{1}{\beta} \ln Tr_1 \, e^{-\beta \tilde{H}_1} - C_2 \frac{1}{\beta} \ln Tr_2 \, e^{-\beta \tilde{H}_2} \qquad (2.1.9)$$

and the condition for a stable value of $\langle J_1 \rangle$ and $\langle J_2 \rangle$ is

$$\frac{\partial F(S_1,S_2)}{\partial S_1} = \frac{\partial F(S_1,S_2)}{\partial S_2} = 0 \; . \qquad (2.1.10)$$

We find that

$$\frac{\partial F(S_1,S_2)}{\partial S_1} = - C_1 \frac{\partial M_1}{\partial S_1} \frac{1}{Z_1} Tr_1 \, J_1 \, e^{-\beta \tilde{H}_1} -$$

$$C_2 \frac{\partial M_2}{\partial S_1} \frac{1}{Z_2} Tr_2 \, J_2 \, e^{-\beta \tilde{H}_2} \qquad (2.1.11)$$

$$= - C_1 \langle J_1 \rangle \frac{\partial M_1}{\partial S_1} - C_2 \langle J_2 \rangle \frac{\partial M_2}{\partial S_1}$$

and a similar expression for $\frac{\partial F}{\partial S_2}$. Tr stands for trace and $Z_i$ is the partition function:

$$Z_i = Tr_i \, e^{-\beta \tilde{H}_i} \; . \qquad (2.1.12)$$

In order to calculate $\frac{\partial M_i}{\partial S_j}$, we have to calculate $\frac{\partial \langle J_i \rangle}{\partial S_j}$. As an example, we find that

$$\frac{\partial \langle J_1 \rangle}{\partial S_1} = \frac{\partial}{\partial S_1} \frac{1}{Z_1} Tr_1 \, J_1 \, e^{-\beta \tilde{H}_1} \qquad (2.1.13)$$

$$= \frac{\partial M_1}{\partial S_1} \left( -\beta \frac{1}{Z_1} Tr_1 \, J_1^2 \, e^{-\beta \tilde{H}_1} + \beta \frac{1}{Z_1^2} Tr_1 J_1 \, e^{-\beta \tilde{H}_1} \, Tr_1 J_1 \, e^{-\beta \tilde{H}_1} \right)$$

$$= \chi_1^o \frac{\partial M_1}{\partial S_1} = \chi_1^o \left( C_1 \tilde{J}^{11} \left( \frac{\partial \langle J_1 \rangle}{\partial S_1} + 1 \right) + C_2 \tilde{J}^{12} \frac{\partial \langle J_2 \rangle}{\partial S_1} \right)$$

by definition of the paramagnetic susceptibility $\chi_1^o$. Inserting this into equation 2.1.11, we find that the condition for an ordered phase is

$$\frac{C_1}{\chi_1^o}\langle J_1\rangle\frac{\partial\langle J_1\rangle}{\partial S_1}+\frac{C_2}{\chi_2^o}\langle J_2\rangle\frac{\partial\langle J_2\rangle}{\partial S_1}=0$$

and (2.1.14)

$$\frac{C_1}{\chi_1^o}\langle J_1\rangle\frac{\partial\langle J_1\rangle}{\partial S_2}+\frac{C_2}{\chi_2^o}\langle J_2\rangle\frac{\partial\langle J_2\rangle}{\partial S_2}=0.$$

In order to obtain solutions apart from the trivial one, we have the condition that

$$\frac{\partial\langle J_1\rangle}{\partial S_1}\frac{\partial\langle J_2\rangle}{\partial S_2}=\frac{\partial\langle J_1\rangle}{\partial S_2}\frac{\partial\langle J_2\rangle}{\partial S_1}. \qquad (2.1.15)$$

By solving the equations of type 2.1.13, we find that

$$\frac{\partial\langle J_1\rangle}{S_1}=\frac{a+\chi_1C_1\tilde{J}^{11}}{1-a}$$

$$\frac{\partial\langle J_2\rangle}{\partial S_1}=\frac{\chi_2C_1\tilde{J}^{12}(1+\chi_1C_1\tilde{J}^{11})}{1-a} \qquad (2.1.16)$$

$$\frac{\partial\langle J_1\rangle}{\partial S_2}=\frac{\chi_1C_2\tilde{J}^{12}(1+\chi_2C_2\tilde{J}^{22})}{1-a}$$

$$\frac{\partial\langle J_2\rangle}{\partial S_2}=\frac{a+\chi_2C_2\tilde{J}^{22}}{1-a}$$

where $a = C_1C_2\chi_1\chi_2(\tilde{J}^{12})^2$. The condition for ordering becomes

$$(a+\chi_1C_1\tilde{J}^{11})(a+\chi_2C_2\tilde{J}^{22})=a(1+\chi_1C_1\tilde{J}^{11})(1+\chi_2C_2\tilde{J}^{22}) \qquad (2.1.17)$$

with the solution

$$a=1 \quad \text{or in other words} \quad \frac{1}{\chi_1}\frac{1}{\chi_2}=C_1C_2(\tilde{J}^{12})^2, \qquad (2.1.18)$$

which is exactly the same condition as equation (2.1.6). Because equations 2.1.16 and 2.1.14 are also valid in the ordered phase, we can calculate ratio of the moments.

$$\frac{C_1 \langle J_1 \rangle}{C_2 \langle J_2 \rangle} = -\frac{\chi_1^o}{\chi_2^o} \chi_2 C_1 \tilde{J}^{12} = \frac{\chi_1^o C_1 \tilde{J}^{12}}{\chi_2^o C_2 \tilde{J}^{22} - 1} . \qquad (2.1.19)$$

As seen, the moments at the two different sites order at the same transition temperature, but if, for instance, $\chi_2^o >> \chi_1^o$ it is more illustrative to state that only $\langle J_2 \rangle$ orders and polarizes $\langle J_1 \rangle$ to a small degree.

The more general case, where $\langle \underline{J}_1 \rangle$ and $\langle \underline{J}_2 \rangle$ are not parallel, can be treated in a similar way. Here it is more convenient to use the molecular field as the order parameter, because the molecular field is equal for each lattice site in a mean field theory. This does not imply that $\langle \underline{J}_1 \rangle$ and $\langle \underline{J}_2 \rangle$ are parallel because they are given by

$$\langle \underline{J}_i \rangle = \tilde{\chi}_i^o \underline{M} . \qquad (2.1.20)$$

This shows that if the molecular field only perturbates the crystal field levels to a small extent, the anisotropy at each atomic site is the same in the alloy as in the pure metal. By generalization of eq. 2.1.18, we find that the condition for ordering is given by

$$\frac{1}{\chi_1^{\alpha\alpha}} \frac{1}{\chi_2^{\alpha\alpha}} = C_1 C_2 (\tilde{J}^{12})^2 . \qquad (2.1.21)$$

From these equations we can calculate the ordering temperatures for ordering in all directions. The highest ordering temperature is the Néel temperature. From equation 2.1.21 it is also seen that the possibility exists of multicritical points. These points are determined by

$$\chi_1^{\alpha\alpha} \chi_2^{\alpha\alpha} = \chi_1^{\beta\beta} \chi_2^{\beta\beta} . \qquad (2.1.22)$$

Equation (2.1.21) can be used to find phase separation lines between two ordered phases if we take the perturbation of the crystal field levels due to the molecular field into account.

This has, of course, to be done by a self-consistent calculation.

In a binary alloy where the magnetic moments order along different directions in the pure elements, there are two interesting cases. If the perturbation of the crystal field levels is weak, the existence of a mixed phase where the moments at the two sites order in different directions is possible. If the perturbation is strong, we can have a first-order transition from an ordered phase with all the moments in one direction to an ordered phase with all the moments in another direction.

## 2.2. Two-ion anisotropy

In the previous section we have neglected two-ion anisotropy. If we neglect single-ion anisotropy, we get a totally different picture of the alloy systems. In the case of a pseudo-dipolar interaction (see sec. 1.1), the total anisotropy energy will be minimized when moments at the two sites are parallel. In the case where the pure elements order along different directions we would expect a gradual change of the direction of ordering across the alloy system.

From spin-wave measurements, Jensen (1975a) was able to calculate the magnitude of the different interactions in Tb. These are

| | |
|---|---|
| Isotropic exchange | 7 meV |
| Two-ion anisotropy | 3 meV |
| Single-ion anisotropy | 3 meV |

The large two-ion anisotropy may indicate that the magnetic structures of the rare earth alloys are homogeneous with a common spin direction. In fact, all earlier measurements can be interpreted if one assumes homogeneous magnetic structures (Millhouse and Koehler 1971, Shirane and Pickart 1966, Spedding et al. 1970).

Lindgård (1976b) recently reanalyzed the spin-wave data. Instead of the Holstein-Primakoff transformation, he used a more correct transformation in order to calculate the spin-wave energy. He was then able to show that the measured spin-wave energies can be explained without inclusion of two-ion anisotropy. This suggests that two-ion anisotropy is at least one order of magnitude smaller than single-ion anisotropy. Our measurements on the Tb-Tm alloys are in agreement with this conclusion.

# 3. EXPERIMENTAL METHOD

## 3.1. Sample preparation

There are several reasons for the difficulty in processing single crystals of the rare earths and their alloys.

a) The rare earth metals are extremely active and in the melted form they react with nearly everything. Care must therefore be taken in the choice of material for the crucible.

b) They may exist in two or more crystal structures (see table 3.1.1).

c) Some of the heavy rare earths and especially Tm are volatile in the molten state (see table 3.1.1).

Table 3.1.1

| | Crystal structures | Melting point in $^{o}C$ | Boiling point in $^{o}C$ |
|---|---|---|---|
| Tb | hcp for T<1287$^{o}C$<br>bcc for T>1287$^{o}C$ | 1360 | 3041 |
| Tm | hcp | 1545 | 1727 |

For these reasons, only the strain anneal method as developed by Nigh (1963) has given successful results (McEwen and Touborg 1973), and the single crystals of Tb-Tm alloys investigated in the present project were prepared by this method.

The first step is to produce a specimen with a considerable number of thermal strains. In the next step the specimen is kept at a temperature as close as possible to the melting point. By this annealing process, the strains in the specimen give rise to the formation of single crystals. Any impurities in the specimen will prevent the growth of single crystals, so every precaution against impurities must be taken during the whole process.

As a first step, Tb and Tm metals of high purity (99.9%) were melted together in the desired proportions by means of arc melting. The crucible was made of copper and water cooled in order to obtain fast cooling. Before melting, the atmospheric air was carefully washed out by argon of high purity (99.999%).

An argon pressure of approximately 1 atm was then established and a Zr specimen was heated up to a temperature just below the melting point. The Zr specimen functioned as an absorber of the impurities that were left in the oven. The Tb-Tm specimens were then carefully melted. The processed specimen had the shape of a button with a diameter of 25 mm and a thickness of 7 mm.

The annealing process took place in an induction furnace. The buttons were suspended by a thin tantalum wire in an open tantalum box. The annealing temperature should be as high as possible, but the hcp-bcc transition must be avoided. Neither may the buttons get so soft that they fall off the tantalum wire. The temperature was determined by an optical pyrometer.

Before the annealing took place the atmospheric air was carefully washed out with argon. Although the final argon pressure was kept at 1 atm, some of the Tm metal evaporated from the buttons. This was perhaps the reason why only small single crystals developed and why we did not succeed in processing single crystal alloys with a Tm content of more than 70%. It has been suggested that the evaporation of Tm can be avoided by welding the tantalum box in an argon atmosphere with a pressure of 1 atm. The large pressure ($\sim$ 5 atm) that develops during the annealing process should then prevent the Tm metal from evaporating.

Figure 3.1.1 shows an example of an annealed button. The temperature has been so high that the button has lost its original form. The grain boundaries are easily seen and a small single crystal was cut from it by means of a spark cutter. The final samples had roughly the shape of a small sphere with a diameter of approximately 1.5 mm. Four samples with Tm concentrations of 12%, 40%, 55%, and 65%, respectively, were prepared. Due to the evaporation of Tm, the actual concentration differed from the nominal. The concentration was determined by an X-ray method.

The samples were oriented by means of X-rays. Figure 3.1.2 shows a Laue picture of the c-axis. The hexagonal symmetry is easily recognized. A small calculation shows that the distance between the spots in fig. 3.1.3 is as expected when an a-axis is in the beam direction and that in fig. 3.1.4 when a b-axis is in the beam direction. Figure 3.1.2 also indicates

Fig. 3.1.1. An annealed button of Tb-40% Tm. The button has been annealed at 1350°C for 4 hours. The grain boundaries between the single crystals are easily seen.

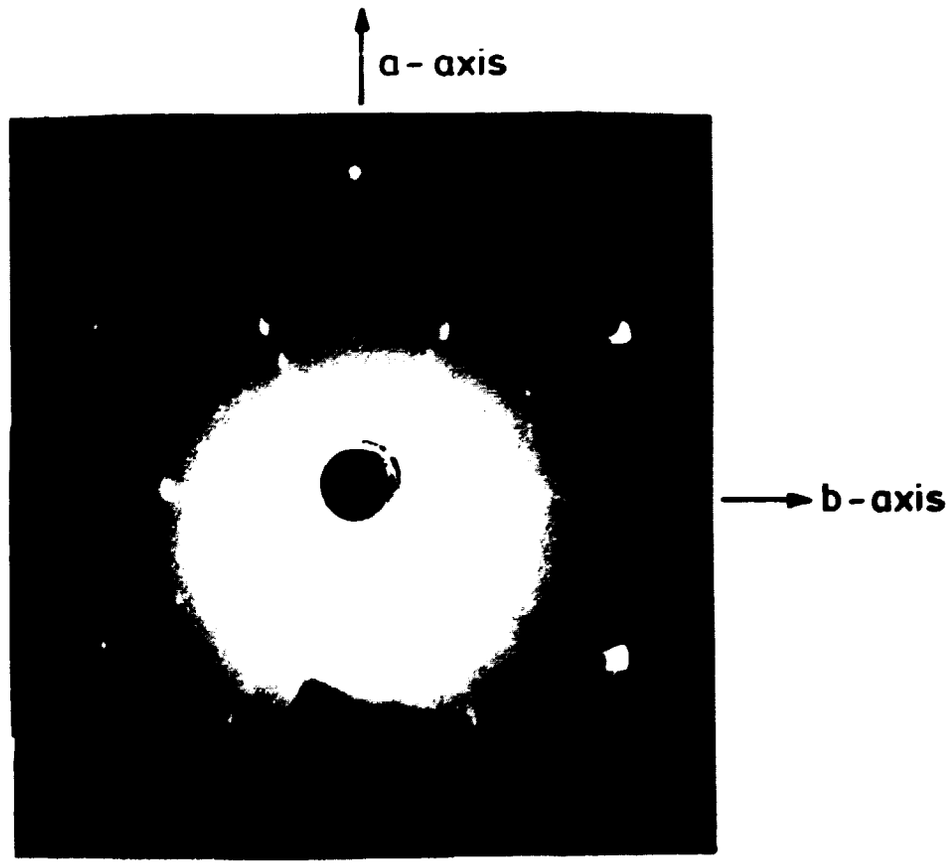


Fig. 3.1.2. A Laue picture with the c-axis of the hcp lattice in the beam direction.

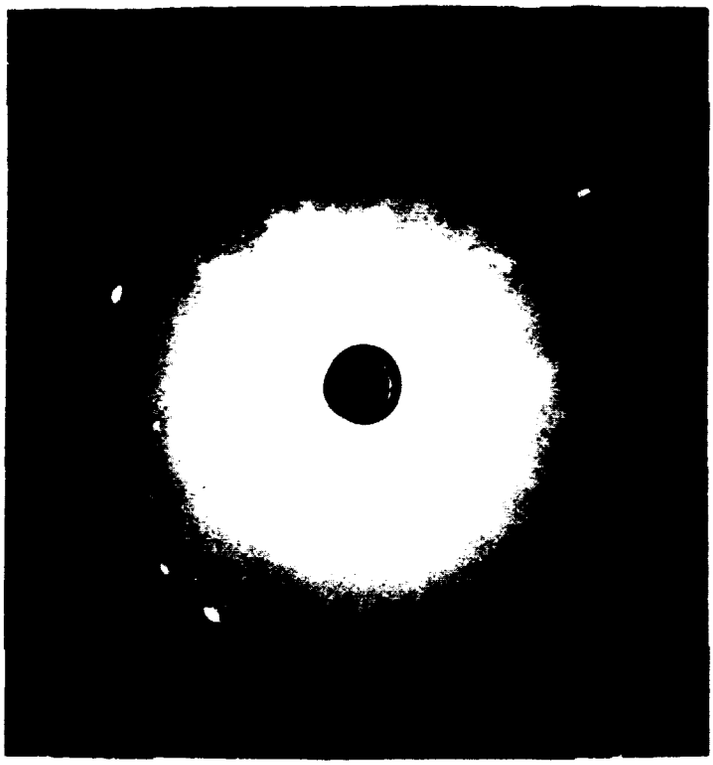

Fig. 3.1.3. A Laue picture with the a-axis of the hcp lattice in the beam direction.

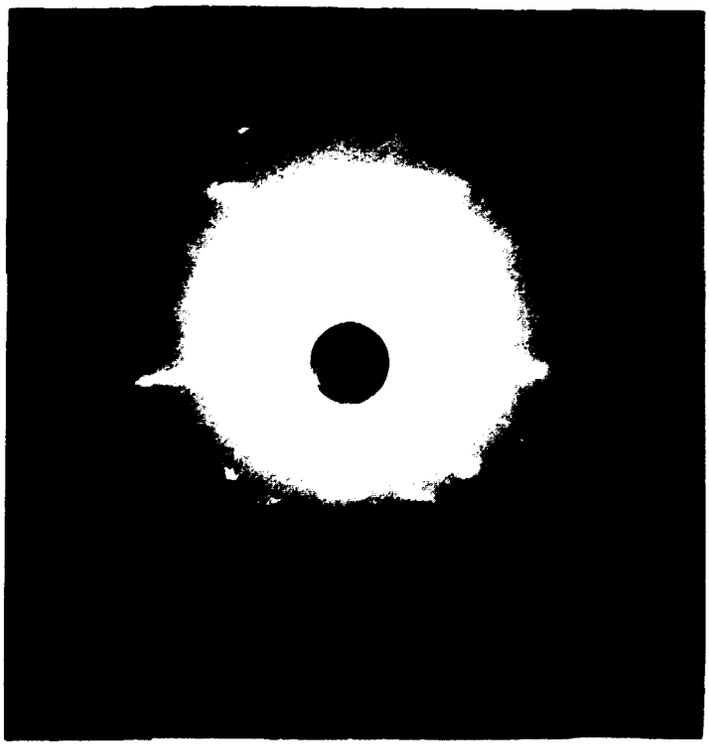

Fig. 3.1.4. A Laue picture with the b-axis of the hcp lattice in the beam direction.

how the a- and the b-axis are easily found once the c-axis is found. A turning of 90 degrees around for instance the a-axis will set the b-axis in the beam direction. The samples were mounted on top of a thin Al-rod for neutron diffraction. The a-axis was chosen parallel to the axis of the Al-rod. The neutron diffraction experiment could then be performed in the b-c plane.

## 3.2. Neutron diffraction techniques

Figure 3.2.1 shows the principle of a neutron diffraction experiment. The sample is exposed to a mono-energetic neutron beam with wave vector $\underline{k}_0$. The scattered neutrons with wave-vector $\underline{k}$ are determined by a detector sensitive to neutrons. The condition for coherent elastic scattering from the lattice is the well-known Bragg equation:

$$n\lambda = 2\,d\,\sin\theta \qquad (3.2.1)$$

where n is an integer, $\lambda$ the wave length ($\lambda=\frac{2\pi}{k}$), d is the distance between the planes of the lattice and $2\theta$ the scattering angle (see fig. 3.2.1). In neutron diffraction one normally uses the more convenient description in terms of reciprocal lattice vectors.

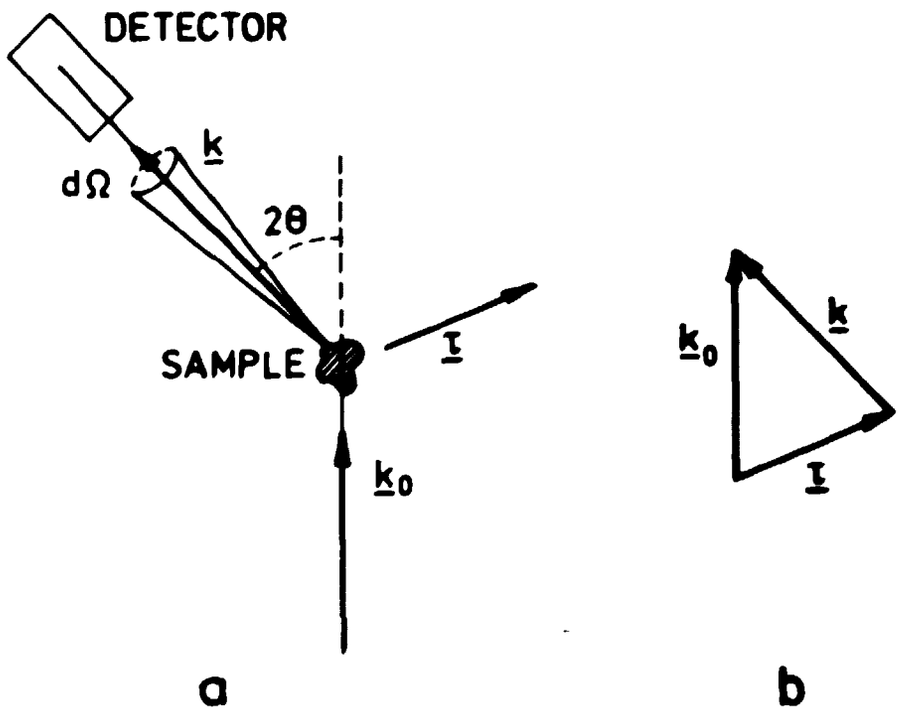


Fig. 3.2.1. The principle of a neutron diffraction experiment.

A reciprocal lattice vector $\underline{\tau}$ is defined as a vector that is perpendicular to the planes of the lattice and has the magnitude $2\pi/d$. The Bragg equation 3.2.1 can in this notation be written in the form

$$\underline{\tau} = \underline{k} - \underline{k}_o = \underline{\kappa}, \tag{3.2.2}$$

where we have defined the scattering vector $\underline{\kappa}$. The n in equation 3.2.1 drops out because $n\underline{\tau}$ is also a reciprocal lattice vector by definition. Figure 3.1.1b is normally referred to as the scattering triangle. As seen, the reciprocal lattice vectors will form a lattice determined by the basis vectors

$$\underline{b}_1 = 2\pi \frac{\underline{a}_2 \times \underline{a}_3}{\underline{a}_1 \cdot (\underline{a}_2 \times \underline{a}_3)}$$

$$\underline{b}_2 = 2\pi \frac{\underline{a}_3 \times \underline{a}_1}{\underline{a}_1 \cdot (\underline{a}_2 \times \underline{a}_3)} \tag{3.2.3}$$

$$\underline{b}_3 = 2\pi \frac{\underline{a}_1 \times \underline{a}_2}{\underline{a}_1 \cdot (\underline{a}_2 \times \underline{a}_3)}$$

The general theory of neutron diffraction has been treated by Marshall and Lovesey (1971). The scattering cross section is defined as

$$\frac{d\sigma}{d\Omega} = \frac{\text{the number of neutrons scattered into the solid angle } d\Omega \text{ per unit time per atom}}{\text{flux of the incident neutrons}}$$

and can be calculated in the Born-approximation for the different scattering processes occurring in the sample.

The interaction between the nuclei and the neutrons can be described by a Fermi pseudo potential

$$V(\underline{r}) = \frac{2\pi\hbar^2}{m} b\, \delta(\underline{r}). \tag{3.2.4}$$

where b is the scattering length. This gives the following result for the elastic scattering

$$\frac{d\sigma}{d\Omega} = b^2 N \frac{(2\pi)^3}{V} e^{-2W} \sum_{\underline{\tau}} |F(\tau)|^2 \delta(\underline{\kappa}-\underline{\tau}). \tag{3.2.5}$$

V is the volume of the unit cell and $F(\underline{\tau})$ is the geometrical structure factor defined as

$$F(\underline{\tau}) = \sum_r \exp(i\underline{\tau}\cdot\underline{d}_r), \tag{3.2.6}$$

where the summation is over all atomic positions $\underline{d}_r$ in the unit cell. The Debye-Waller factor $e^{-2W}$ enters into equation 3.2.5 because the atoms oscillate around the position of equilibrium. $e^{-2W}$ can be calculated in a harmonic approximation for cubic symmetry. The result is

$$W(\underline{\kappa}) = \frac{\hbar^2\kappa^2}{2M}\,\frac{3k_BT}{(k_B\theta_D)^2}\,\left(1 + \frac{1}{36}\left(\frac{\theta_D}{T}\right)^2 - \frac{1}{3600}\left(\frac{\theta_D}{T}\right)^4\right) \tag{3.2.7}$$

if the phonon spectrum is assumed to be a Debye spectrum. The result is also a good approximation in symmetries other than the cubic one. The symbols used in eq. 3.2.7 are defined on p. 7.

If the sample consists of more than one isotope, the scattering amplitude has to be exchanged by its mean value

$$\langle b\rangle = \sum_i c_i b_i \tag{3.2.8}$$

in the expression for the cross section (eq. 3.2.5). $c_i$ is the concentration of the isotopes. In this case an additional term enters into the cross ection,

$$\left(\frac{d\sigma}{d\Omega}\right)_{inc} = N(\langle b^2\rangle - \langle b\rangle^2). \tag{3.2.9}$$

Because this term is purely incoherent, it only adds a constant background to the coherent scattering and we will not consider it any further.

If the atom has a magnetic moment, this will give rise to a magnetic scattering. The energy of a neutron with spin $\underline{\sigma}_n$ in a magnetic field $\underline{H}$ is given by

$$E_m = -\gamma\underline{\sigma}_n \cdot \underline{H}, \tag{3.2.10}$$

where $\gamma$ is the gyromagnetic moment of the neutron. Hence, there

is an interaction between the neutron and the unpaired electrons. The elastic coherent cross section for magnetic scattering is given by

$$\left(\frac{d\sigma}{d\Omega}\right)_{mag} = \frac{1}{N}\left|\sum_{\ell} \underline{E}_{\ell} \exp(i\underline{\kappa} \cdot \underline{R}_{\ell})\right|^2 \qquad (3.2.11)$$

where the summation is over all atoms, their positions given by $\underline{R}_{\ell}$. In this case the scattering process is described by a vector defined as

$$\underline{E}_{\ell} = p\, f_{\ell}(\underline{\kappa})\, \hat{\kappa} \times (\underline{\mu}_{\ell} \times \hat{\kappa}) \qquad \hat{\kappa} \equiv \frac{\underline{\kappa}}{|\underline{\kappa}|} \qquad (3.2.12)$$

$\underline{\mu}_{\ell}$ is the moment at site $\underline{R}_{\ell}$ and p is sometimes called the magnetic scattering amplitude.

$$p = \tfrac{1}{2} r_o \gamma = 0.269\ 10^{-12}\ \text{cm} \qquad (3.2.13)$$

where $r_o$ is the classical electron radius. $\underline{E}_{\ell}$ depends on the spatial extent of the unpaired electron density through the magnetic form-factor $f(\underline{\kappa})$, which is the Fourier transform of the spin density $u_{\ell}(\underline{r})$ associated with the ion at the $\ell$'th site in the lattice:

$$f_{\ell}(\underline{\kappa}) = \int u_{\ell}(\underline{r})\, e^{i\underline{\kappa} \cdot \underline{r}} d\underline{r} \,. \qquad (3.2.14)$$

In the dipole approximation the expression for the magnetic form-factor is

$$f(\underline{\kappa}) = \langle j_o \rangle + \frac{J(J+1) + L(L+1) - S(S+1)}{3J(J+1) + S(S+1) - L(L+1)} \langle j_2 \rangle \qquad (3.2.15)$$

where

$$\langle j_{\ell}(\kappa) \rangle = \int_o^{\infty} r^2 |g(r)|^2 B_{\ell}(\kappa r) dr \qquad (3.2.16)$$

g(r) is the r-dependence of the wave function and $B_{\ell}(\kappa r)$ is a Bessel function of order $\ell$. If use is made of the Freeman and Watson one-electron wave function, then g(r) for the 4f orbitals is given by (Freeman and Watson 1962)

$$g(r) = \sum_{i}^{4} C_i r^4 e^{-Z_i r} \,. \qquad (3.2.17)$$

The parameters $Z_i$ and $C_i$ for Tb and Tm are given in table 3.2.1.

Table 3.2.1

| | Tb | | Tm | |
|---|---|---|---|---|
| | $Z_i$ | $C_i$ | $Z_i$ | $C_i$ |
| 1 | 13.009 | 2182.9 | 14.831 | 3494.3 |
| 2 | 7.288 | 385.86 | 8.258 | 689.52 |
| 3 | 4.858 | 49.188 | 5.505 | 80.645 |
| 4 | 2.67 | 1.9118 | 3.020 | 4.0735 |

The explicit expressions for the integrals in equation 3.2.16 are (Lander and Brun 1973),

$$\langle j_o \rangle = \sum_{i,j}^{4} N_{ij}(1-7x_{ij} + 7x_{ij}^2 - x_{ij}^3)/(1 + x_{ij})^8$$

$$\langle j_2 \rangle = \sum_{i,j}^{4} N_{ij}6x_{ij}(1- \frac{10}{7} x_{ij} + \frac{5}{21} x_{ij}^2)/(1 + x_{ij})^8 \qquad (3.2.19)$$

where

$$N_{ij} = \frac{8!C_iC_j}{(Z_i+Z_j)^9} \qquad (3.2.20)$$

and

$$x_{ij} = (\frac{\kappa}{Z_i + Z_j})^2 \ . \qquad (3.2.21)$$

By combining equations 3.2.19 and 3.2.15, we are able to calculate the magnetic form factor.

In order to find a more explicit expression for the magnetic cross section, we have to set up a magnetic model. The Tb-Tm data could be understood on the basis of the following model with $\underline{Q}$ parallel to the c-axis

$$\mu_{nx} = \mu_{\perp} \cos \underline{Q} \cdot \underline{R}_n$$

$$\mu_{ny} = \mu_{\perp} \sin \underline{Q} \cdot \underline{R}_n \qquad (3.2.22)$$

$$\mu_{nz} = \mu_{||} + A_{||} \cos \underline{Q} \cdot \underline{R}_n$$

The $\mu_{||}$ term allows for a ferromagnetic component along the c-axis. In this case, the cross section has the form

$$\frac{d\sigma}{d\Omega} = N\frac{(2\pi)^3}{V} p^2 f^2(\underline{\kappa}) e^{-2W} \frac{1}{4} (\mu_{\perp}^2(1+\cos^2\phi)+A_{||}^2\sin^2\phi)$$

$$\times \sum_{\underline{\tau}} |F(\underline{\tau})|^2(\delta(\underline{\kappa} + \underline{Q} - \underline{\tau}) + \delta(\underline{\kappa} - \underline{Q} - \underline{\tau})) \qquad (3.2.23)$$

$$+ N \frac{(2\pi)^3}{V} p^2 f^2(\underline{\kappa}) e^{-2W} \mu_{||}^2 \sin^2\phi \sum_{\underline{\tau}} |F(\underline{\tau})|^2\delta(\underline{\kappa}-\underline{\tau})$$

where $\phi$ is the angle between the scattering vector $\underline{\kappa}$ and the c-axis. As seen, the modulated part of the magnetic moments gives rise to magnetic satellites displaced $\underline{Q}$ from the nuclear Bragg reflections, while a ferromagnetic component gives additional scattering to the nuclear Bragg reflections. The directional parameter $\phi$ in equation (3.2.23) makes it possible to deduce the direction of the magnetic moments. The magnitudes of the moments can be calculated from the integrated intensities of the magnetic peaks. If a coarse collimation is used in front of the counter, it is simple to calculate the integrated intensity by means of equation (3.2.23) (Lebech and Nielsen 1975). The result is

$$I_{sat}(\underline{\tau} \pm \underline{Q}) = C p^2|f(\underline{\tau} \pm \underline{Q})|^2 e^{-2W} \frac{1}{4}(\mu_{\perp}^2(1 + \cos^2\phi) + A_{||}^2\sin^2\phi) \frac{|F(\tau)|^2}{|\sin(\theta-\alpha)|} \qquad (3.2.24)$$

for the magnetic satellites, and

$$I_{ferro}(\underline{\tau}) = C p^2|f(\underline{\tau})|^2 e^{-2W} \mu_{||}^2 \sin^2\phi \times \frac{|F(\tau)|^2}{|\sin(\theta-\alpha)|} \qquad (3.2.25)$$

for the ferromagnetic intensity. C is a scale factor and $\alpha$ is the angle between the reciprocal lattice vector and the scan direction.

In the case of unpolarized neutrons, the magnetic and nuclear scattering cross sections simply add up

$$\frac{d\sigma}{d\Omega} = \left(\frac{d\sigma}{d\Omega}\right)_{nuc} + \left(\frac{d\sigma}{d\Omega}\right)_{mag} . \qquad (3.2.26)$$

Hence, a ferromagnetic component is determined as the difference in the intensity above and below the ordering temperature. The integrated intensity of the nuclear scattering is given by

$$I_{nuc}(\underline{\tau}) = C \frac{b^2 e^{-2W} |F(\tau)|^2}{|\sin(\theta-\alpha)|} . \qquad (3.2.27)$$

The scattering amplitudes for Tb, Tm and Nd are given in table 3.2.2.

Table 3.2.2

| | Tb | Tm | Nd |
|---|---|---|---|
| b($10^{-12}$ cm) | 0.76 | 0.69 | 0.72 |

By measuring the nuclear intensities, we are able to determine the scale factor C, and from equations (3.2.24) and (3.2.25) we can then calculate the absolute value of the magnetic moments.

## 3.3. Description of the neutron diffractometer

The experiments were made at Risø using the double-axis neutron spectrometer TAS V. This spectrometer is mounted at one of the tangential beam holes of the DR 3 reactor. It is shown in figures 3.3.1 and 3.3.2.

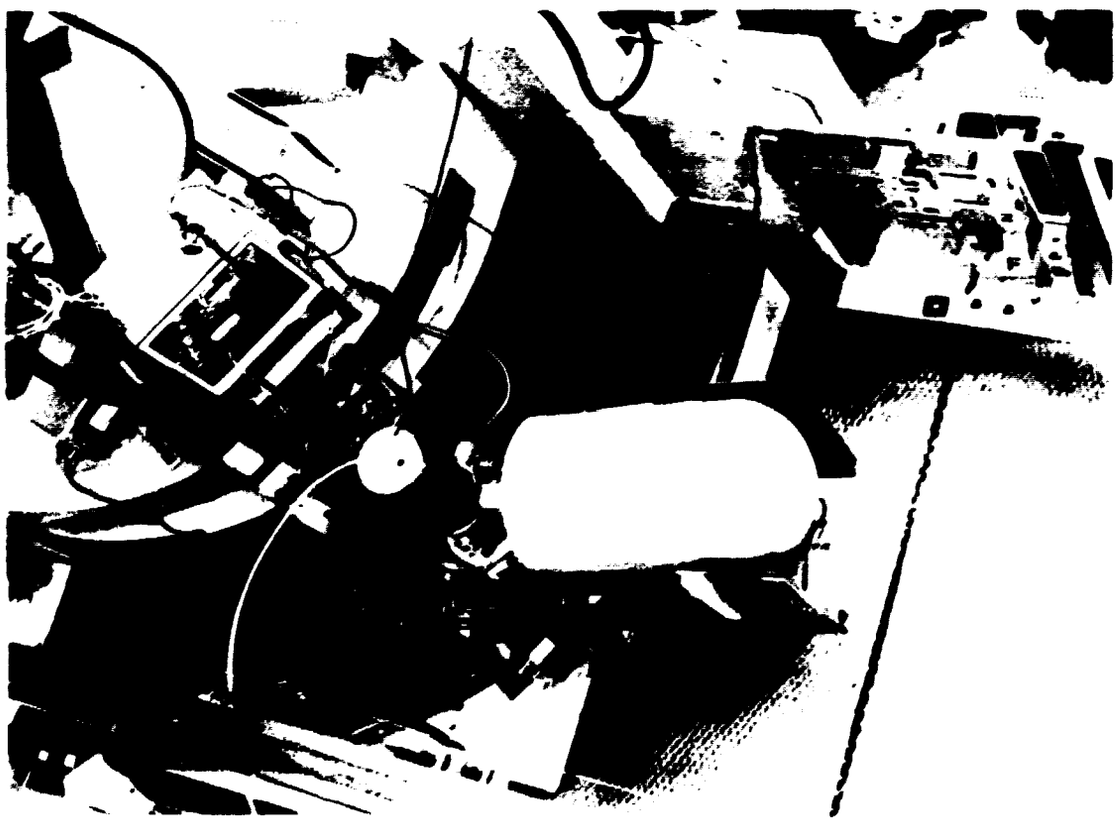

Fig. 3.3.1. The neutron diffractometer TAS V.

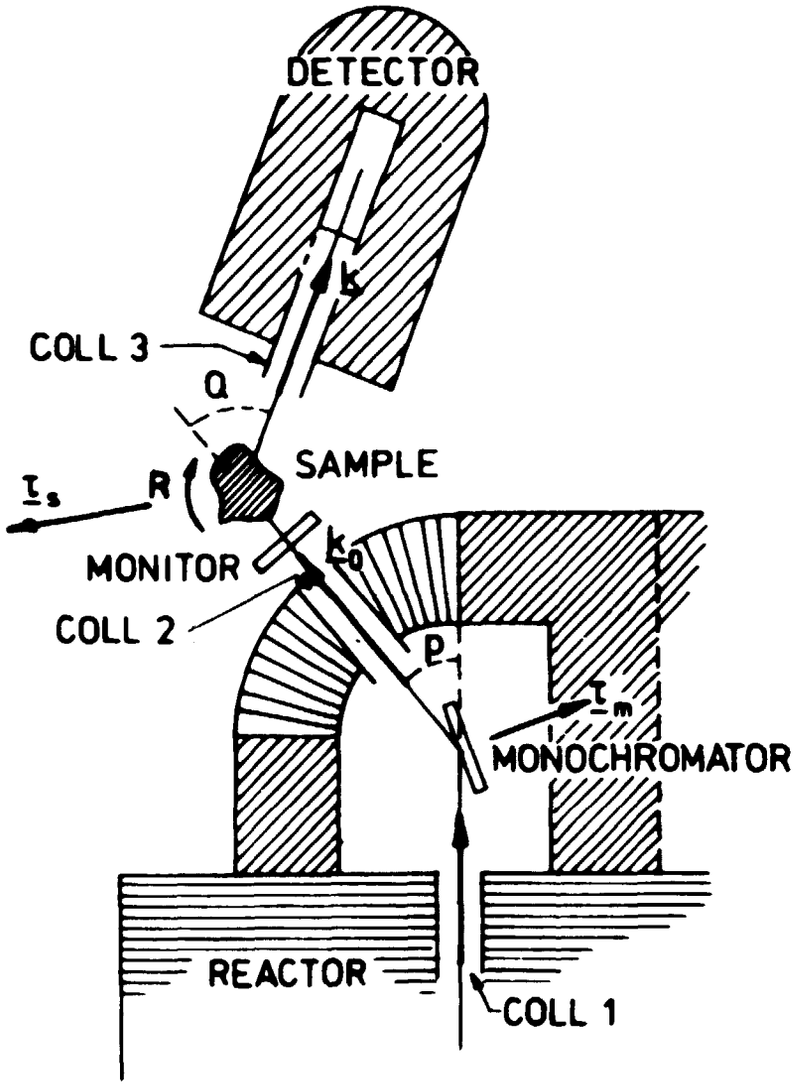


Fig. 3.3.2. The principle of the neutron diffractometer.

The polyenergetic neutron beam incident upon the monochromator crystal is obtained from a water scatterer placed in the beam tube at the position of the maximum thermal flux ($\sim 6 \times 10^{13}$ n/cm$^2$ s). The hydrogen cross section is 80 barns for thermal neutrons, while that of fast neutrons is 20 barns. By a suitable choice of the thickness of the water scatterer, it is therefore possible to obtain a thermalized neutron beam with very little contamination of fast neutrons. The energy spectrum of the neutrons at the beam hole is approximately a Maxwellian distribution with maximum at 25 meV.

The monoenergetic neutron beam is produced by the monochromator system. This consists of a monochromator crystal and two multichannel collimators (Soller collimators) which define the direction of the neutron beam. The collimation defined by the collimators can be changed by removing or adding plates. A

large single crystal of Ge (60 mm x 60 mm x 8 mm) was used as monochromator crystal. The scattering in this crystal was from the (111) planes. Since (222) is a forbidden reflection, second-order contamination of the neutron beam was avoided. Third and higher-order contamination could be neglected because of the Maxwellian distribution of the incident neutrons. The energy of the monoenergetic beam can be changed by changing the scattering angle in the monochromator system, or by changing to another monochromator crystal.

The detector is a gas counter filled with $BF_3$ gas. It has the shape of a cylinder with a long axis (5 cm x 30 cm) in order to obtain a high efficiency. The detector is well shielded in order to limit the background from external sources. Between the monochromator and the sample is placed a low efficiency $He^3$ monitor. Hence the counting time can be determined by the number of incident neutrons, so that the results are independent of fluctuations in the incident beam. The sample was mounted on a goniometer so that it could be precisely aligned. For the low temperature measurements, the sample was placed inside a cryostat which could be filled with either liquid nitrogen or helium. Temperatures from liquid helium temperature (4.2 K) and upwards could be reached by applying current to heating coils placed in thermal connection with the sample. The temperature was measured by a GaAs sensor and controlled by a feed-back system. The temperature was kept within approximately $\pm$ 0.1 K.

All the angles (P, Q and R, see fig. 3.3.2) at the spectrometer can be read to an accuracy of one hundredth of a degree. The Q and R angles are set in position by step motors. The operation of the spectrometer is automated by a PDP8-computer. Specified scans through the different elastic reflections are easily performed and the temperature can also be set automatically. The results are punched on paper tape that can be used in processing the experimental data.

## 3.1. Experimental problems

Normally there is no resolution problem in diffraction experiments on single crystals. In the case of Tb-Tm and Nd, the magnetic sattellites were well separated from the nuclear Bragg

reflection and they were easily resolved, but in the case of MnSi we had to use neutrons of very long wavelength before we could resolve the satellites properly (see chap. 6).

The worst problem in doing diffraction experiments on single crystals is that of extinction. This effect is caused by the fact that the incident beam does not penetrate the whole sample due to Bragg reflection. Neutron scattering is normally encountered as a volume effect, but if we deal with a large perfect crystal and consider a strong reflection, only the front part of the crystal will be exposed to neutrons because they are scattered away from the incident beam. On the other hand, a larger part of the crystal will contribute to the scattering of neutrons in the case of a weak reflection. Hence, the measured intensity of a strong and of a weak reflection may be almost equal. This effect is normally referred to as primary extinction. Primary extinction is not so important as it might seem at first, because real crystals are not perfect but consist of small domains of perfect crystals which are slightly misorientated. In this case there is the possibility that some domains have the same orientation, and if the crystal is large they may be so numerous that extinction again becomes a problem. This is called secondary extinction and may be avoided by using a sufficiently small crystal. Both the Tb-Tm samples and the Nd sample were so small that we were unable to measure any extinction effect, but in the case of MnSi we were forced to use a large crystal because the magnetic reflections were very weak (see chap. 6).

# 4. Tb-Tm ALLOY SYSTEM

## 4.1. Introduction

The results presented in this chapter has also been published in J.Phys.F. (Hansen and Lebech 1976). The main purpose of the investigation of the Tb-Tm alloys was to study the magnetic anisotropy of the rare earths.

Tb and Tm have very different magnetic anisotropy. In fact, Tb is the rare earth where the magnetic moment is most strongly bound to the basal plane, and Tm the one where the magnetic moment is most strongly bound to lying along the c-axis of the hcp lattice. The possible magnetic structures of a Tb-Tm alloy much depend, as discussed in sec.2.2, on which of the two possible sources of magnetic anisotropy is dominant. Single-ion anisotropy will result in an inhomogeneous structure where the magnetic moments of the Tb-ions point in a direction different to that of the Tm-ions. In contrast, two-ion anisotropy will result in a structure where all the moments point in the same direction.

All earlier experiments on the magnetic structure of binary rare earth alloys may be interpreted if one assumes homogeneous structures (Millhouse and Koehler 1971, Shirane and Pickart 1966 and Spedding et al. 1970), but due to the experimental error, there is the possibility that the magnetic moments of the two types of ions make a small angle with each other. However, the experimental results discussed in this chapter unambiguously show that the magnetic structures of the Tb-Tm alloys are inhomogeneous, and we conclude that single-ion anisotropy is the dominant source of anisotropy in the rare earths. Before proceeding to the experimental results (sec. 4.3), the magnetic structures of pure Tb and pure Tm will be discussed in sec. 4.2.

## 4.2. Magnetic properties and structures of pure Tb and pure Tm

Like the rest of the heavy rare earths, Tb and Tm crystallize in the hexagonal close-packed structure (hcp) (see fig. 4.2.1), and they form perfect solid solutions with each other. The crystallographic parameters for Tb and Tm are given in table 4.2.1.

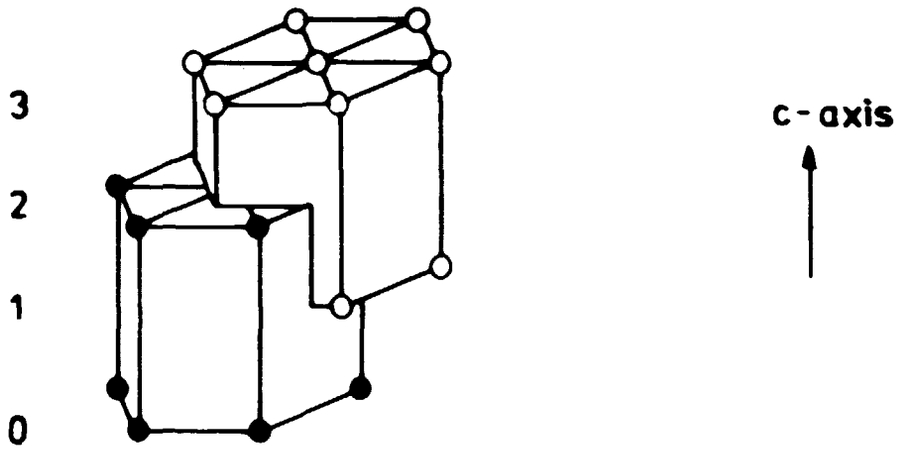


Fig. 4.2.1. The hexagonal close-packed (hcp) structure.

Table 4.2.1

| | a | c |
|---|---|---|
| Tb | 3.6010 Å | 5.6936 Å |
| Tm | 3.5375 Å | 5.5546 Å |

The magnetic properties of the rare earths are mainly determined by the quantum numbers of the magnetic ground state L, S, and J (see chapter 1). These quantum numbers are determined by Hunds' rules: S is maximum and L is maximum provided that S is maximum. J equals L+S, if the shell is more that half-full and L-S if the shell is less that half-full. Table 4.2.2 gives the principal quantum numbers, the Landé factor

$$g = 1 + \frac{J(J+1) + S(S+1) - L(L+1)}{2J(J+1)} \qquad (1.2.1)$$

and furthermore the expectation value of the magnetic moment gJ in units of the Bohr magneton and the ground levels for the $3^+$-ions.

The magnetic structures of the heavy rare earths are shown in figure 1.1.1 (Koehler 1972). The moments have equal size and point in the same direction within each layer perpendicular to the hexagonal axis. The figure shows how the magnetic moments change on going from one layer to the next.

Terbium: The magnetic structure of Tb was first investigated by Koehler et al. (1963). Tb is highly anisotropic with the magnetic moments confined to the basal plane at all tem-

Table 4.2.2

| | No. of 4f-electrons | ground level | L | S | J | g | gJ |
|---|---|---|---|---|---|---|---|
| $Tb^{3+}$ | 8 | $^7F_6$ | 3 | 3 | 6 | $\frac{3}{2}$ | 9 |
| $Tm^{3+}$ | 12 | $^3H_6$ | 5 | 1 | 6 | $\frac{7}{6}$ | 7 |

peratures. Below the Néel temperature (230 K), the magnetic moments are ordered as a basal plane spiral (see fig. 1.1.1e). The interlayer turn angle, which describes the turning of the moments from one layer to the next layer, varies with temperature from 20°/layer to 18°/layer. At the Curie temperature (220 K) this structure transforms into a ferromagnetic structure with the magnetic moments in the basal plane (fig. 1.1.1f). The magnetic moments then point in the easy b-direction. The saturation value of the magnetic moments is 9.34 $\mu_B$/atom. This is in good agreement with the expectation value gJ = 9.0 $\mu_B$/atom, the small difference being due to a polarization of the conduction electrons.

Thulium: Tm has also been investigated by Koehler et al. (1962). Like Tb, Tm is highly anisotropic with the moments constrained to lie along the c-axis. The antiferromagnetic structure below the Néel temperature (57.2 K) is shown in fig. 1.1.1b. This structure is called the c-axis modulated structure (CAM-structure). The angle that describes this structure is nearly constant at 50°/layer. This structure persists until the temperature at which the amplitude of the modulation saturates. When the amplitude of the modulation exceeds 7.0 $\mu_B$, the structure must change and it does. In neutron spectra, higher harmonics are observed than the fundamental harmonics. This "squaring-up" of the moments continues down to 4.2 K, where the antiphase structure with 4 moments up and 3 moments down is stable (see fig. 1.1.1a). The net moment per atom is 7.14 $\mu_B$, which should be compared with the expectation value gJ = 7.0 $\mu_B$. The difference is also in this case believed to be due to a polarization of the conduction electrons.

## 4.3. Description of the experimental results

The samples which were used in the investigation of the Tb-Tm alloys were processed as described in sec. 3.1. The magnetic structures of the alloys were investigated by means of neutron diffraction (see sec. 3.2).

In order to investigate whether extinction (see sec. 3.3) is of any importance, the intensities of fourteen nuclear reflections were measured above the ordering temperature. For the hcp-lattice, the squares of the geometrical structure factors of the allowed reflections are 1, 3 and 4. As no systematic trend was seen in the observed structure factors, we conclude that extinction is negligible for nuclear scattering. The R-factors obtained for the nuclear scattering were $\sim$ 3%, where R is defined as

$$R = \frac{\Sigma\left|\,|F_{obs}|^2 - |F_{cal}|^2\,\right|}{\Sigma|F_{cal}|^2}$$

The summation is over all the measured reflections. $|F_{obs}|^2$ and $|F_{cal}|^2$ are the observed and calculated structure factors, respectively. Because the intensities of the magnetic reflections at low temperature are of the same order of magnitude as the nuclear reflections, extinction is also unimportant for magnetic scattering.

Scans were performed along the symmetry directions of the lattice in search of magnetic scattering. Because the modulation vector $\underline{Q}$ for all the heavy rare earth metals is parallel to the c-axis, we expect this to be true also for their alloys and, indeed, this was found to be correct. In fig. 4.3.1 is shown an example of a scan parallel to the c-axis through the (100) reflection. The magnetic satellites on each side of the nuclear Bragg reflections are easily seen. We denote these satellites $(h,k,\ell)\ \pm$. The intensities of the satellites and the $(h,k,\ell)$ reflections were measured as a function of temperature between 4.2 K and the ordering temperature.

As an example, we consider the results for the Tb-55% Tm alloy. Magnetic satellites, such as those in fig. 4.3.1, begin to develop below $145^{\circ}$ K around every nuclear reflection. As there is no change in the intensity at the reciprocal lattice points at this transition temperature, the magnetic structure

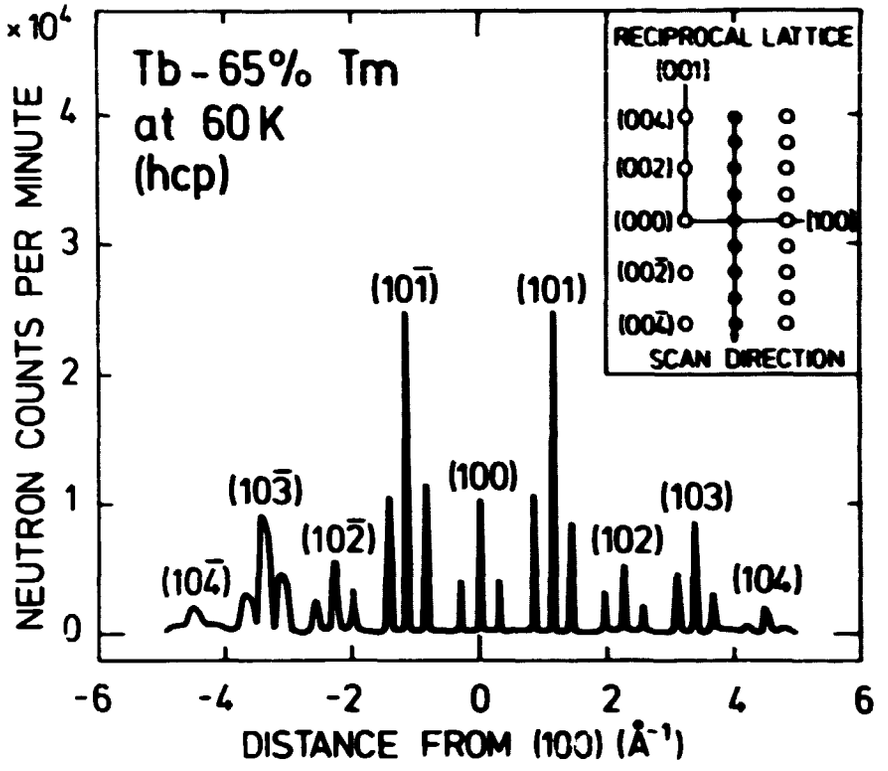


Fig. 4.3.1. A scan through the (100) reflection parallel to the c-axis. The nuclear reflections are indicated in the figure. The magnetic satellites around each nuclear reflection are easily seen. The magnetic structure of Tb-65% Tm is a basal plane spiral at 60 K.

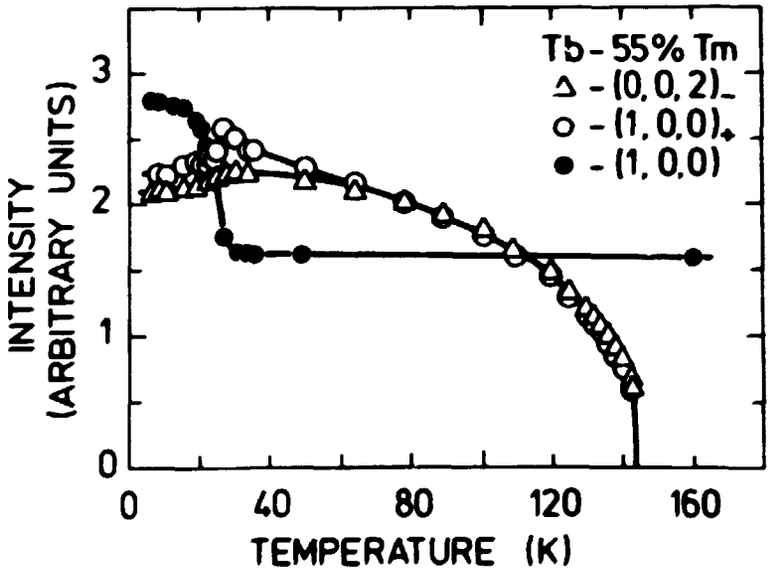


Fig. 4.3.2. The intensities of the (100), $(100)_+$, and $(002)_-$ reflections as measured on the Tb-55% Tm alloy. The intensity of the $(100)_+$ satellite is multiplied by $8 \times (1 + \cos^2\phi)$ and coincides with the intensity of the $(002)_-$ satellite at high temperature. The difference between the two satellites at low temperature shows the existence of the $A_{II}$-term. The additional scattering in the (100) reflection at low temperature is caused by a ferromagnetic component $\mu_{II}$

is antiferromagnetic. The intensity of the $(100)_+$, $(002)_-$ and the (100) reflections is shown in fig. 4.3.2 as a function of temperature. When the magnetic structure is a basal plane spiral, we find from equation 3.2.24 that

$$\frac{I(002)_-}{I(100)_+} = \left(\frac{f(002)_-}{f(100)_+}\right)^2 8(1 + \cos^2\phi) \sim 8(1 + \cos^2\phi) \qquad (4.3.1)$$

$f(002)_- \sim f(100)_+$, because the lengths of the scattering vector for the $(002)_-$ and $(100)_+$ reflections are approximately the same. In fig. 4.3.2 we have multiplied the intensity of the $(100)_+$ reflection by $8(1 + \cos^2\phi)$. Between 145 and 35 K this scaled intensity coincides with the intensity of the $(002)_-$ reflection. Hence the magnetic structure is a basal plane spiral at high temperatures. The deviation of the scaled intensities at low temperature shows the development of a modulated component along the c-axis, as easily seen from equation 3.2.24. Below 30 K, this modulated component turns ferromagnetic as seen from the increase in the intensity of the (100) reflection and the decrease in the intensity of the $(100)_+$ reflection. This ferromagnetic component is along the c-axis because there is no change in the intensities of the (00ℓ) reflections. Perhaps the modulated component along the c-axis does not completely disappear, as seen from the small difference between the scaled intensities of the $(100)_+$ and the $(002)_-$ reflections at temperatures below 30 K.

This interpretation of the results is only valid if the magnetic structure can be written in the form given in equation 3.2.22. The validity of this equation was examined by measuring the intensity of several reflections at selected temperatures, and a detailed analysis is given in tables 4.3.1 and 4.3.2. The magnetic structure factors were calculated from the measured intensities using both the experimentally found form factors for pure Tb (Brun and Lander 1969) and Tm (Brun and Lander 1971), and those calculated from the Freeman and Watson wave functions as outlined in sec. 3.2. In a preliminary analysis a mean form factor was used. As we shall see below, the moments in the basal plane are alone due to the Tb-spins and the moments along the c-axis to the Tm-spins. In the final analysis we therefore used the Tb form factor to calculate the basal plane moments and the Tm form factor to calculate the c-axis moment. The

Table 4.3.1

| (h,k,ℓ) | $\mu_\perp$(8.0K) ($\mu_B$) | $\mu_{eff}$(30.7K) ($\mu_B$) [a] | $\mu_\perp$(30.7K) ($\mu_B$) [b] | $A_{\parallel}$(30.7K) ($\mu_B$) | $\mu_\perp$(58.2K) ($\mu_B$) |
|---|---|---|---|---|---|
| (1,0,-1)- | 3.96±.1 | 5.50±.1 | (4.22±.1) | 2.72±.7 | 3.67±.1 |
| (1,0,-1)+ | 4.06±.1 | 5.33±.1 | (4.22±.1) | 2.94±.5 | 3.72±.1 |
| (1,0,0)- | 4.21±.1 | 5.48±.1 | (4.22±.1) | 3.35±.3 | 3.83±.1 |
| (1,0,0)+ | 4.18±.1 | 5.54±.1 | (4.22±.1) | 3.46±.3 | 3.93±.1 |
| (1,0,1)- | not measured | 5.46±.1 | (4.22±.1 | 3.18±.4 | 3.83±.1 |
| (1,0,1)+ | 3.90±.1 | 5.57±.1 | (4.22±.1 | 3.14±.6 | 3.81±.1 |
| (0,0,2)- | 4.05±.1 | 4.25±.1 | 4.25±.1 | 0 | 3.87±.1 |
| (0,0,2)+ | 3.93±.1 | 4.13±.1 | 4.13±.1 | 0 | 3.79±.1 |
| (0,0,4)- | 3.94±.1 | not measured | not measured | 0 | 3.98±.1 |
| (0,0,4)+ | 3.80±.1 | 4.28±.1 | 4.28±.1 | 0 | 4.06±.1 |
| Weighted mean $\mu_\perp$ | 4.00±.1 | | 4.22±.1 | 3.18±.3 | 3.85±.1 |
| R | 4.5% | | 3.0% | | 5.2% |

The magnetic moment $\mu_\perp$ and the amplitude $A_{\parallel}$ of the Tb-65% Tm alloy at different temperatures as calculated from different magnetic satellites. The R-factor is calculated by using the weighted mean values given in the table.
a) $\mu_{eff} = \{\mu_\perp^2(1 + \cos^2\phi) + A_{\parallel}^2 \sin^2\phi\}^{\frac{1}{2}}$,
b) $\mu_\perp$ at 30.7 K is determined as the weighted mean value of $\mu_\perp$ at 30.7 K of the (001) ± satellites.

Table 4.3.2

| (h,k,ℓ) | (1,0,-4) | (1,0,-3) | (1,0,-2) | (1,0,-1) | (1,0,0) | (1,0,1) | (1,0,2) | (1,0,3) | (1,0,4) | $\mu_{\parallel}(\mu_B)$ weighted mean | R |
|---|---|---|---|---|---|---|---|---|---|---|---|
| $\mu_{\parallel}(\mu_B)$ | 4.40±1 | 4.31±.7 | 4.36±.4 | 4.47±.3 | 4.68±.2 | 4.61±.3 | 4.59±.4 | 4.94±.8 | 5.17±1 | 4.58±.2 | 3.6% |

The ferromagnetic component $\mu_{\parallel}$ of the Tb-65% Tm alloy at 5.8 K as calculated from different nuclear reflections. The R-factor is calculated by using the weighted mean values given in the table.

measured intensities were in best agreement with the calculated form factor. We also searched carefully for higher-order satellites, but none were found.

The temperature dependence of the magnetic moments is shown in fig. 4.3.3. The magnetic structure of the Tb-65% Tm and the

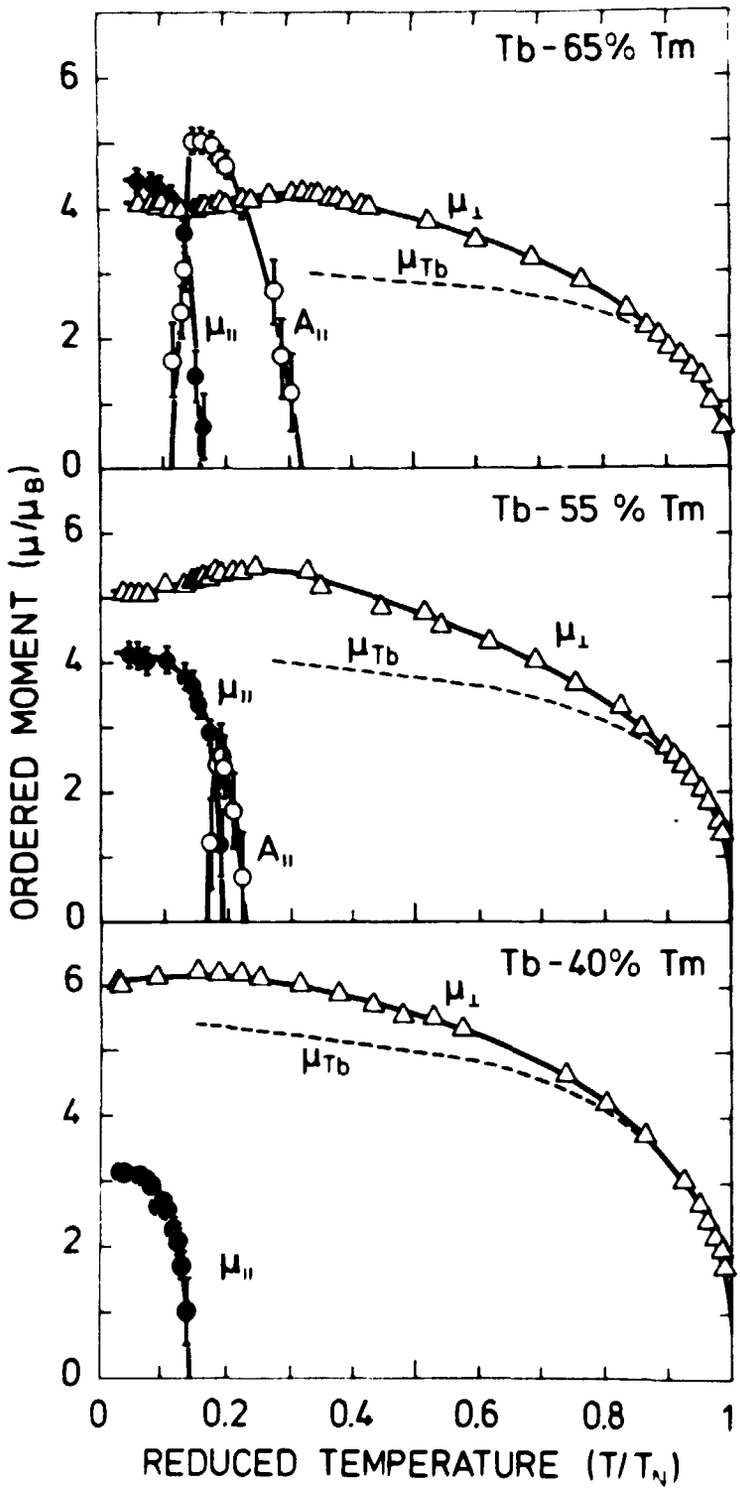


Fig. 4.3.3. The magnetic components of the Tb-65% Tm alloy, the Tb-55% Tm alloy and the Tb-40% Tm alloy as function of reduced temperature. $\mu_{\perp}$ is the spiral component in the basal plane, $A_{||}$ is the amplitude of the sine-modulated component along the c-axis, and $\mu_{||}$ is the ferromagnetic component parallel to the c-axis. The broken lines show the magnetic moment as measured on pure Tb (Dietrich and Als-Nielsen 1967) scaled by the concentration.

Tb-40% Tm alloys is similar to that of the Tb-55% Tm alloy, but the sine modulated phase is widest in the Tb-65% Tm alloy and has completely disappeared in the Tb-40% Tm alloy.

The Tb-12% Tm single crystal alloy was a rather imperfect crystal and it was impossible to make reliable measurements of its integrated intensity. It was, however, possible to deduce the magnetic structure, which was found to be similar to that of Tb with the moments in the basal plane at all temperatures. The only difference between the Tb-12% Tm alloy and pure Tb is that the temperature range in which the helix structure exists is wider in the alloy. The phase diagram for the Tb-Tm alloy system, as deduced from these four alloys and the pure elements, is shown in fig. 4.3.4.

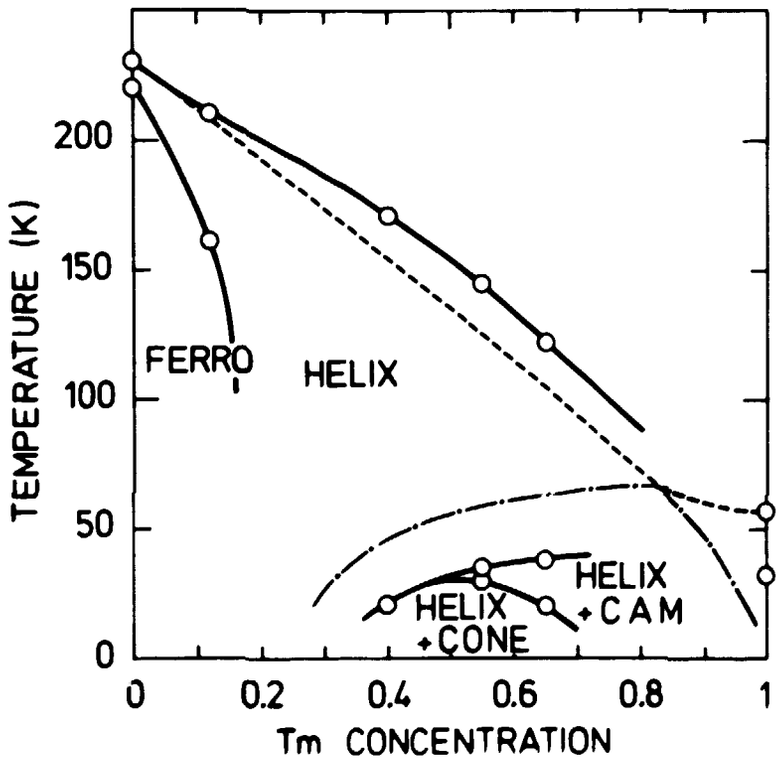


Fig. 4.3.4. The phase diagram of the Tb-Tm alloy system. The mixed phases are labelled helix + CAM and helix + cone. The dashed and dot-dashed lines are calculated as described in the text.

The important question is of course: are we able to deduce the magnitude and the directions of the Tb spins and the Tm spins in these alloys? If the Tb and Tm spins are parallel, the total moment would be given by

$$\mu_T = (\mu_{||}^2 + \mu_\perp^2)^{\frac{1}{2}} \quad \text{or} \quad \mu_T = (\tfrac{1}{2}A_{||}^2 + \mu_\perp^2)^{\frac{1}{2}} \qquad (4.3.2)$$

depending on the magnetic structure. Table 4.3.3 lists the values of $\mu_T$ at 4.2 K. As seen, these values are all below the expected value because that of Tm is 7 $\mu_B$ and that of Tb is 9 $\mu_B$.

Table 4.3.3

| | $T_{n,N}$(K) | T'(K) | $T_C$(K) | $\mu_{||}(\mu_B)$ | $\mu_\perp(\mu_B)$ | $\mu_T(\mu_B)$ | $\phi_{Tb}$(DEG) | $\phi_{Tm}$(DEG) | $\omega_i$(DEG) |
|---|---|---|---|---|---|---|---|---|---|
| Tb | 230 a) | | 220 a) | 0 | 9.32 a) | | | | 20.5 a) |
| Tb-12%Tm | 210±1 | | 161±1 | | | | | | 31.6±.2 |
| Tb-40%Tm | 171±1 | | 21±2 | 3.15±.2 | 6.06±.2 | 6.83±.3 | 86.6±2.5 | 9.39±4.5 | 42.1±.2 |
| Tb-55%Tm | 145±1 | 35±1 | 30±1 | 4.14±.2 | 5.07±.2 | 6.55±.3 | 85.7±4.0 | 13.0±4.0 | 46.2±.2 |
| Tb-65%Tm | 122±1 | 38±1 | 20±1 | 4.58±.2 | 4.07±.2 | 6.13±.3 | 89.8±4.5 | 9.9±2.5 | 48.6±.2 |
| Tm | 57.2 b) | | 32 b) | 7.14 b) | | | | | 51 b) |

Summary of the transition temperatures ($T_N$, T', and $T_C$), the turn angle ($\omega_i$) just below the Néel temperature, and the ordered moments ($\mu_\perp$, $\mu_{||}$, and $\mu_T=(\mu_\perp^2+\mu_{||}^2)^{\frac{1}{2}}$). T' is the temperature at which the c-axis component starts to oscillate. $\phi_{Tm}$ and $\phi_{Tb}$ are the angles between the c-axis and the Tm and Tb moments, respectively.

a) from Koehler et al. (1963),

b) from Koehler et al. (1962).

Hence, the Tb and Tm spins cannot be parallel. As seen from figure 4.3.5, $\mu_T$ has a kink at the ordering temperature of the c-axis component and this effect cannot be explained if we assume a homogeneous structure. The measured values of the magnetic moments are in much better agreement with the assumption that the Tb spins lie in the basal plane and the Tm spins along the c-axis. We may calculate the angles made by the Tb spins and the Tm spins with the c-axis at 4.2 K in the alloys, if we adopt the values 9.34 $\mu_B$ and 7.14 $\mu_B$ for the fully ordered moment of the Tb and Tm spins, respectively. These values include the contribution from the conduction electrons. The calculated angles are $\sim 85^\circ$ for the Tb spins and $\sim 10^\circ$ for the Tm spins (see table 4.3.3); within the experimental error the lower limit of the angle between the Tb and Tm spins is $65^\circ$.

Table 4.3.3 lists the main results of the measurements. The Néel temperatures closely follow the experimentally found law

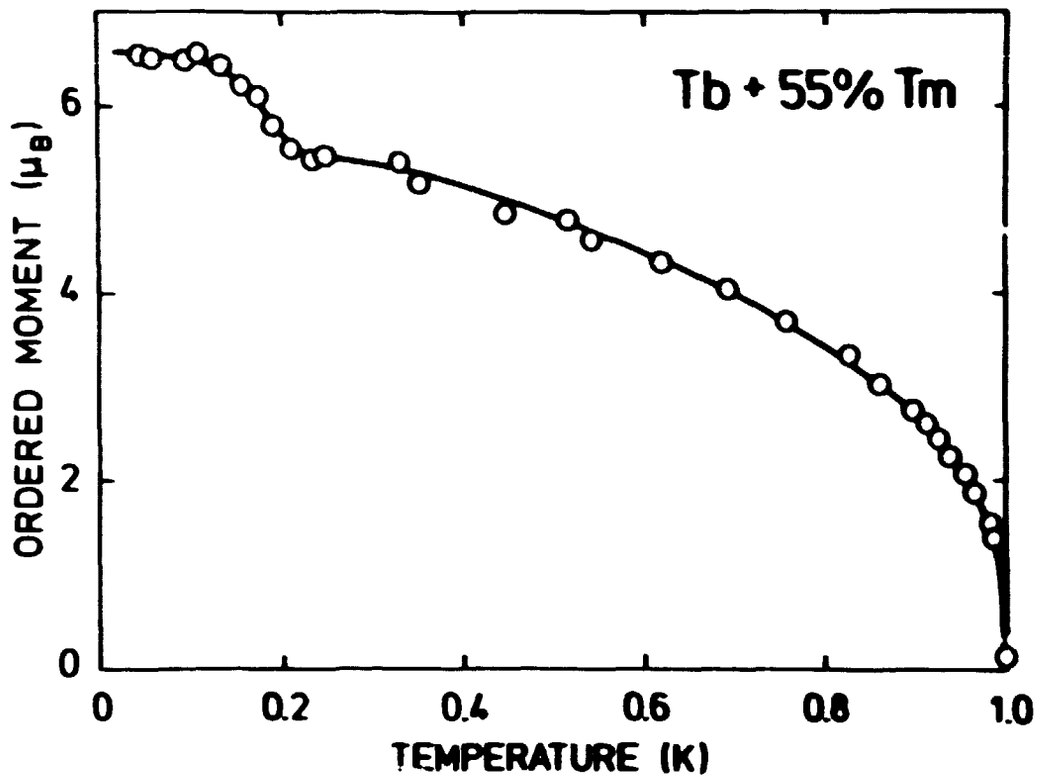


Fig. 4.3.5. The total moment $\mu_T$ calculated as $\mu_T = (\mu_\perp^2 + \mu_{||}^2)^{\frac{1}{2}}$ or $\mu_T = (\mu_\perp^2 + A_{||}^2)^{\frac{1}{2}}$ depending on the magnetic structure as function of reduced temperature for the Tb + 55% Tm alloy.

that $T_N = 46.7\ G^{2/3}$ (Bozorth 1967), which is valid for all other heavy rare earth metals and their alloys so far measured. G is the Néel-De Gennes factor, defined as

$$G = \sum_i C_i (g_i - 1)^2 J_i (J_i + 1)$$

where the summation is over all different ions in the alloy. The modulation vector just below the transition temperature is also a smoothly varying function of the Néel-de Gennes factor, and the values found in this experiment are in good agreement with the previous experiments (Koehler 1972). The modulation vector was deduced from the separation of the magnetic satellites. The results are given as a function of reduced temperature in fig. 4.3.6 together with the modulation vectors of pure Tb and pure Tm. As seen, the modulation vector changes gradually from that of Tb to that of Tm across the alloy system. It is noticed that the modulation vector is the same for the $\mu_\perp$-term and the $A_{||}$-term.

The phase transition from a modulated component to a ferromagnetic component along the c-axis occurs because the amplitude of the modulation cannot exceed 7.0 $\mu_B$. This is similar to the case of pure Tm, although we do not observe a "squaring-up" of the moments, but an abrupt change resulting in a ferromagnetic component of the moments. The model in which the Tb and Tm

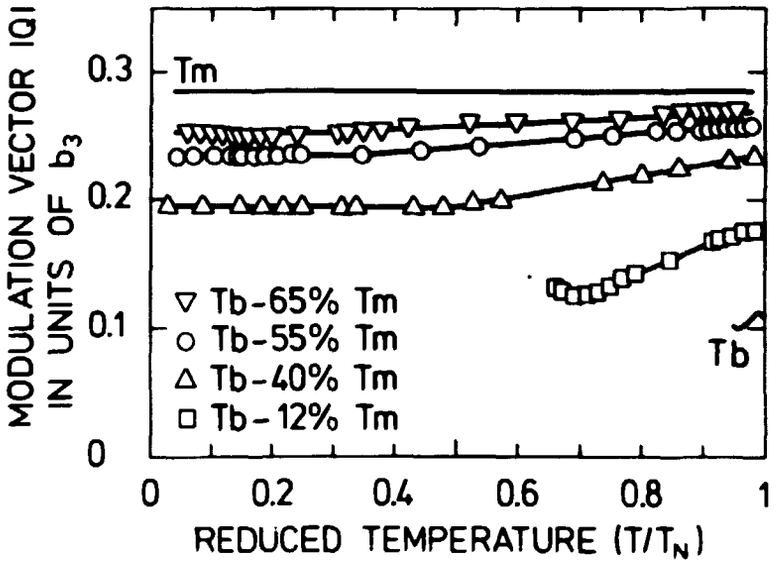


Fig. 4.3.6. The modulation vector as function of reduced temperature. The modulation vector for the pure elements is taken from the measurements by Koehler et al. (1963 and 1962). The modulation vector changes gradually from that of Tb to that of Tm.

spins are perpendicular to each other is only valid for the concentrated alloys. In the Tb-12% Tm alloy the Tb and Tm spins are parallel, and this is expected to be true for the diluted alloys at both ends of the alloy system because of the strong molecular field of the host material.

It is reasonable to compare $\mu_\perp(T)$ with the temperature dependence of the magnetic moment of pure Tb at temperatures above the ordering temperature for the c-axis component. The magnetic moment of pure Tb has been measured by Als-Nielsen and Dietrich (1967) and is shown as the dashed line in fig. 4.3.3, where it has been scaled by the Tb-concentration. The difference between this curve and $\mu_\perp(T)$ is presumably due to a small polarization of the Tm spins. As seen, the polarization is less than 1 $\mu_B$.

The Néel temperatures were deduced from measurements of the magnetization as function of temperature using a Foner magnetometer. The external magnetic field was 3 kGauss. The transition temperatures found by this method were in good agreement with the neutron diffraction results, although weak magnetic satellites were detected above the Néel temperature. The satellite

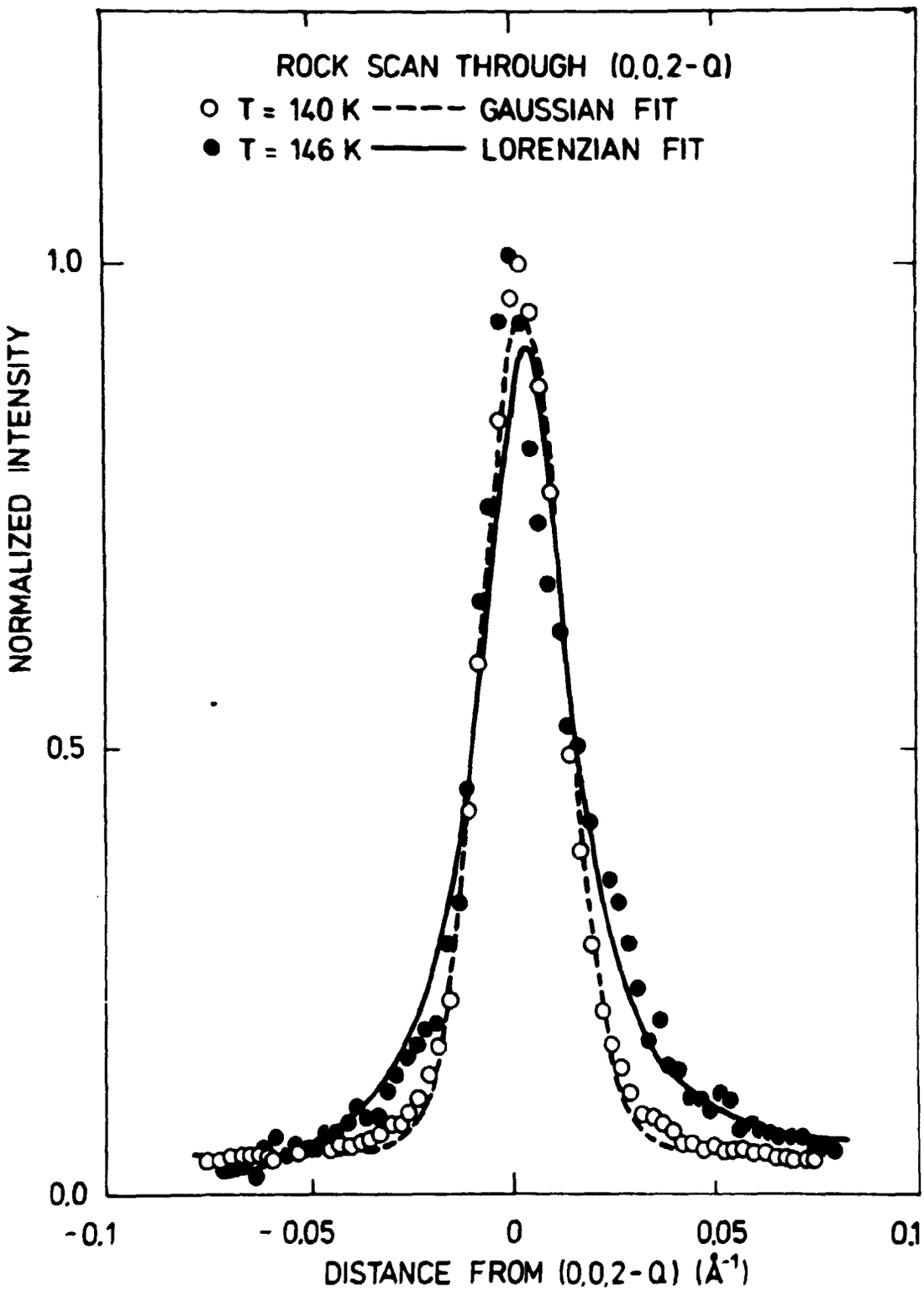


Fig. 4.3.7. Scans through the (0,0,2-Q) satellite of the Tb + 55% Tm alloy above and below the Néel temperature (143 K). The lines show the results of a fit to a Lorenzian and a Gaussian curve, respectively. The Lorenzian shape indicates critical scattering.

peaks were much broader above the transition temperature and they had a Lorentzian distribution as seen in fig. 4.3.7. This indicates that the scattering results from critical scattering, which is caused by concentration gradients or clustering of the Tb ions. A similar effect was seen at the ordering temperature for the c-axis component (see fig. 4.3.8).

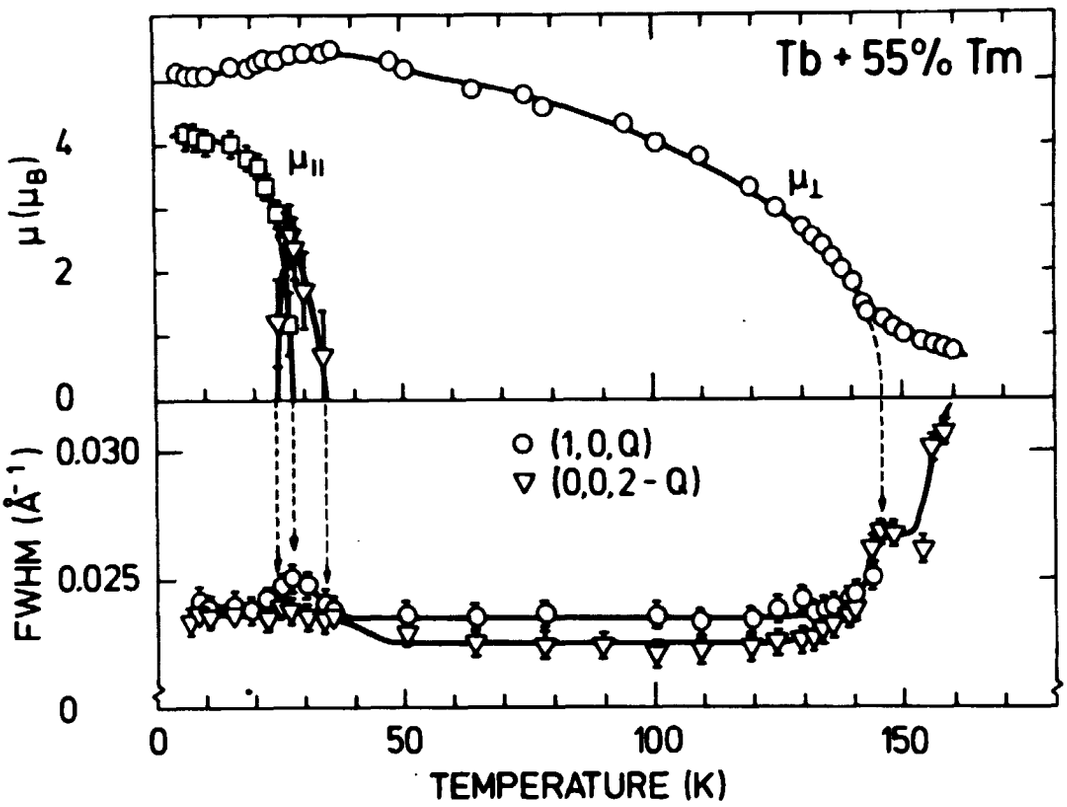


Fig. 4.3.8. The upper part is a repetition of a part of fig. 4.3.3. The lower part shows the full width at half maximum (FWHM) of the (1,0,Q) and the (0,0,2-Q) satellites as function of temperature. The change of the FWHM at the phase transitions is easily seen.

## 4.4. Discussion of the experimental results

The description of the experimental results in section 4.3 gives the following picture of the Tb-Tm alloy system. The diluted alloys have magnetic structures similar to those of the host material and the helical structures are stabilized over a wider temperature range. The concentrated alloys have more complicated magnetic structures and a sketch of these structures is shown in fig. 4.4.1. Just below the Néel temperature, only the magnetic moments of Tb are ordered, and the Tm moments are polarized to a small extent. At low temperatures, the Tm spins order in a direction almost perpendicular to the Tb spins. The Tm spins lie on a cone with a small cone angle, while the Tb

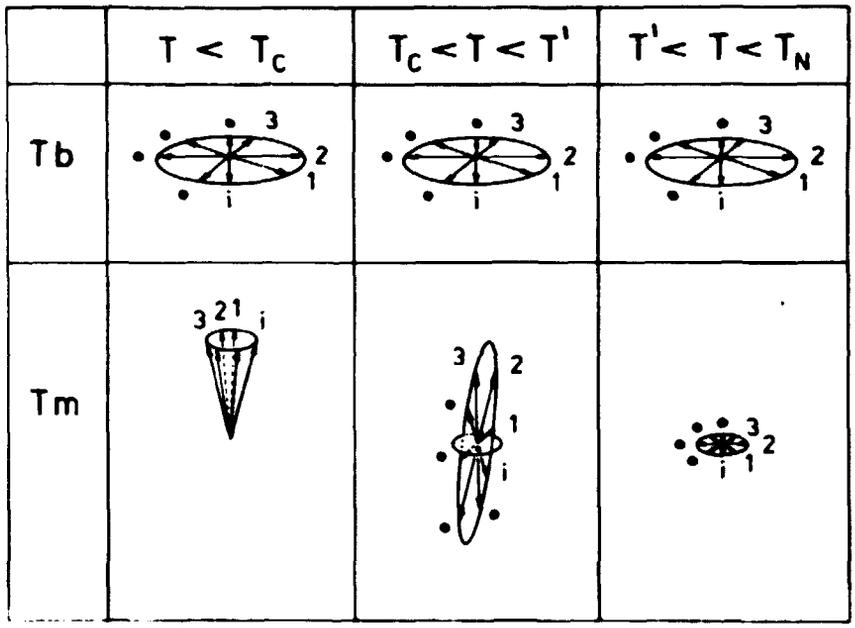


Fig. 4.4.1. The figure shows a sketch of how the magnetic structures of the concentrated alloys are formed by the Tb and Tm spins. The magnetic moments are projected on to the same hexagonal plane and are shown in a perspective view. The numbers refer to different hexagonal layers. The upper row shows the Tb-moments that are ordered as a basal plane spiral. The ordering may be a flat cone at low temperature. The lower row shows the Tm-moments, which are polarized at high temperature and are ordered as a cone structure with a small opening angle at low temperatures. There may be an intermediate structure where the Tm-moments lie at a tilted ellipse as shown in the middle column.

spins are ordered almost as a basal plane spiral. In Tb-55% Tm and Tb-65% Tm there is an intermediate phase at higher temperatures, where the Tm moments lie on a tilted ellipse with the long axis almost parallel to the c-axis. These observations are in good agreement with the theory outlined in sec. 2.1, where only single-ion anisotropy was included.

The crystal field levels for the Tb and the Tm ions may be simplified by taking only the lowest levels into account. Hence, Tb is a singlet-doublet system, and Tm a singlet-singlet system. The non-vanishing matrix elements of the paramagnetic susceptibility are therefore

$$\chi_{Tb}^{xx} = \chi_{Tb}^{yy} \quad \text{and} \quad \chi_{Tb}^{zz} \quad \text{for Tb}$$

$$\chi_{Tm}^{zz} \quad \text{for Tm} \qquad (4.4.1)$$

Hence, by use of equation 2.1.6, we find that the Néel temperature is given by

$$\left(\frac{1}{\chi^{zz}_{Tm}} - c\mathcal{J}_{TmTm}\right)\left(\frac{1}{\chi^{zz}_{Tb}} - (1-c)\,\mathcal{J}_{TbTb}\right) = \mathcal{J}^2_{TbTm}c(1-c)) \qquad (4.4.2)$$

and

$$\frac{1}{\chi^{xx}_{Tb}} - (1-c)\,\mathcal{J}_{TbTb} = \mathcal{J}^2_{TbTm}\,c(1-c)\,\frac{\chi^{xx}_{Tm}}{1-\chi^{xx}_{Tm}c\mathcal{J}_{TmTm}} = 0 \qquad (4.4.3)$$

depending on which of these equations gives the highest and therefore the real Néel temperatures. The dashed lines in fig. 4.3.4 are calculated from these equations. The direction of the moments just below the transition temperature is given by the equations above, which means that the ordering is in the basal plane at the Tb-rich end of the system and along the c-axis at the other end. The small polarization of the Tm ions, which was seen in the experimental results, comes from the fact that $\chi^{xx}_{Tm}$ has a small value if we include the higher crystal field levels.

As mentioned in sec. 2.1 are equation (4.4.2) and (4.4.3) valid below the Néel temperature if the perturbation of the crystal field levels due to the molecular field is taken into account. Hence by means of these equations we can calculate the transition temperature below which a mixed phase exist. The Tb-spins and the Tm-spins will order in nearly perpendicular directions because

$$\chi^{xx}_{Tb} >> \chi^{xx}_{Tm} \quad \text{and} \quad \chi^{zz}_{Tm} >> \chi^{zz}_{Tb}\ . \qquad (4.4.4)$$

There are no fitting parameters in the calculation of the phase separation lines in fig. 4.3.4. The crystal field parameters have been determined by Touborg (1976). The exchange constants for the pure elements are calculated from the Néel temperatures, and $\mathcal{J}_{TbTm}$ is obtained from scaling by an effective factor $f^2$

$$J_{Tb}:J_{TbTm}:J_{Tm} = 1:f:f^2\ . \qquad (4.4.5)$$

If the Néel-de Gennes scaling was correct, $f^2$ should be given by

$$f^2 = [(g_{Tm} - 1)/(g_{Tb} - 1]^2 \qquad (4.4.6)$$

We have also tried to use $J_{TbTm}$ as a fitting parameter. With a value which is 1.89 larger than that obtained by the Néel-de Gennes scaling, we find full agreement with the measured Néel temperatures, but simultaneously the calculated transition temperature, at which the transition into the mixed phase occurs, gets higher.

As seen, this simple model is in really good qualitative agreement with the experimental results. The quantitative agreement is not too poor either, and there may be several reasons for the discrepancy. The worst shortcoming is probably that the q-dependence of the exchange constants is neglected. As seen from fig. 4.3.6, there is a drastic change in the modulation vector across the alloy system, but it is difficult to include this effect because we only know the q-dependence of the exchange constant for Tb. It is at least not reasonable to include a large two-ion anisotropy, because we would then get an alignment of the two different kinds of spins.

## 4.5. Conclusion

Measurements on Tb-Tm alloys have unambiguously showed the existence of an inhomogeneous magnetic structure. The measurements are in qualitative agreement with calculations that include isotropic exchange and single-ion anisotropy and utilize parameters determined from other experiments. As mentioned in sec. 2.2, this picture of the origin of the anisotropy is supported by a recent reanalysis of the spin wave energies in Er. The calculation of the phase diagram for the Tb-Tm alloy system indicates the existence of a tetra critical point, which it would be very interesting to investigate.

# 5. MAGNETIC STRUCTURE AND CRITICAL BEHAVIOUR OF Nd

## 5.1. Introduction

The crystallographic structure of Nd is the double hexagonal close-packed structure (dhcp) shown in fig. 5.1.1. The arrows on this figure indicate the magnetic structure proposed by Moon

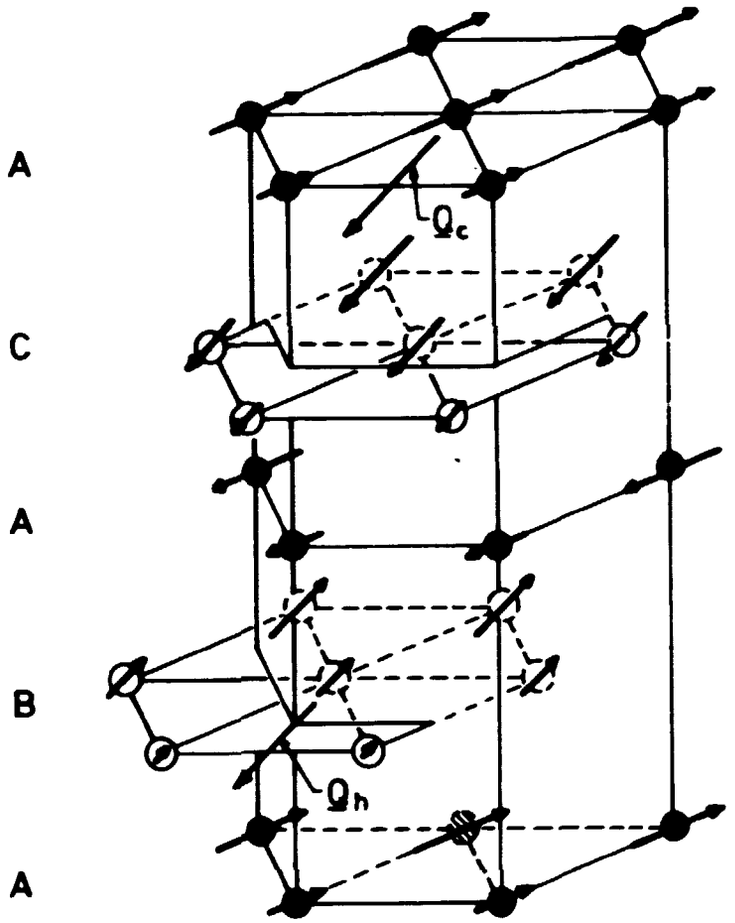


Fig. 5.1.1. The double hexagonal close-packed structure of Nd. The arrows indicate the magnetic structure proposed by Moon et al. (1964).

et al. (1964). We will return to this structure below. The dhcp structure has the very interesting feature that there are two different sites in it. The stacking sequence along the c-axis is ABAC. Considering only the nearest neighbours, the atoms in the A layers have nearly cubic surroundings, while the atoms in the B and C layers have hexagonal surroundings. If, as concluded in sec. 4.5, the magnetic anisotropy is a crystal field effect, we would expect the magnetic behaviour of the ions at the cubic sites to differ from that of the ions at the hex-

agonal sites. Indeed, this is the case, as we shall see below. Furthermore, we would expect the magnetic behaviour to be very similar to the Tb-Tm case, in the sense that the theory outlined in sec. 2.1 is valid for both cases. Although we are not able to prove this in detail, there is no contradictory evidence in our results.

It would, of course, be very interesting to investigate the critical behaviour of these mixed systems. Unfortunately, the Tb-Tm samples were too small for these studies, but in the case of Nd we were able to measure the critical exponent. The measured value for $\beta(0.5)$ is very remarkable, but we do not know why because we have not yet found the right description of the magnetic structure of Nd.

Section 5.2 describes the model for the magnetic structure as proposed by Moon et al. (1964) and the shortcoming of this model in the light of our measurements (Lebech and Hansen 1977). Section 5.3 describes the measurements of the critical behaviour of Nd.

## 5.2. Magnetic structure of Nd

The magnetic structure of Nd was first investigated by Moon et al. (1964) and they suggested the following model (see fig. 5.1.1). Below 19 K, the moments at the hexagonal sites are ordered. The moments in the B and C layers are given by

$$\underline{\mu}_B = \hat{b}\mu_h \cos \underline{Q}_h \cdot \underline{R}_{nB}$$

and

$$\underline{\mu}_C = -\hat{b}\mu_h \cos \underline{Q}_h \cdot \underline{R}_{nC}$$

$\hat{b}$ is a unit vector along the b-direction (see fig. 5.1.1). The moments at the cubic sites order at 7 K and are given by

$$\underline{\mu}_A = \hat{a}\mu_c \cos \underline{Q}_c \cdot \underline{R}_{nA} \qquad (5.1.2)$$

and

$$\underline{\mu}_{A'} = -\hat{a}\mu_c \cos \underline{Q}_c \cdot R_{nA'} \cdot$$

By use of equation 3.2.11 we can calculate the elastic coherent cross section of the magnetic scattering. The result is

$$\frac{d\sigma}{d\Omega} = \frac{N}{V(2\pi)^3} p^2 f^2(\underline{\kappa}) \frac{1}{4} \mu_c^2 \sin^2\phi_c |G_c|^2$$

$$\times \sum_{\underline{\tau}} \delta(\underline{\kappa} + \underline{Q}_c - \underline{\tau}) + \delta(\underline{\kappa} - \underline{Q}_c - \underline{\tau})$$

$$+ \frac{N}{V(2\pi)^3} p^2 f^2(\underline{\kappa}) \frac{1}{4} \mu_h^2 \sin^2\phi_h |G_h|^2 \qquad (5.1.3)$$

$$\times \sum_{\underline{\tau}} \delta(\underline{\kappa} + \underline{Q}_h - \underline{\tau}) + \delta(\underline{\kappa} - \underline{Q}_h - \underline{\tau})$$

$\phi_c$ and $\phi_h$ are the angles between the scattering vector and the moments at the cubic sites and at the hexagonal sites, respectively. The position of the atoms in the lattice cell is given by

$$\begin{aligned} \underline{d}_1 &= (0,0,0) && \text{(A-layer)} \\ \underline{d}_2 &= (1/3,2/3,1/4) && \text{(B-layer)} \\ \underline{d}_3 &= (0,0,1/2) && \text{(A'-layer)} \\ \underline{d}_4 &= (2/3,1/3,3/4) && \text{(C-layer)} \end{aligned} \qquad (5.2.4)$$

In this notation the geometric structure factors $|G_h|^2$ and $|G_c|^2$ are given by

$$|G_h|^2 = |e^{i\underline{\tau}\cdot\underline{d}_2} - e^{i\underline{\tau}\cdot\underline{d}_4}|^2 = 2[1-\cos(\tfrac{2}{3}h - \tfrac{2}{3}k + \ell)\pi] \qquad (5.2.5)$$

$$|G_c|^2 = |e^{i\underline{\tau}\cdot\underline{d}_1} - e^{i\underline{\tau}\cdot\underline{d}_3}|^2 = 4 \sin^2 \frac{\pi}{2} \ell \qquad (5.2.6)$$

The magnetic satellites are detected in accordance with these structure factors, but the model cannot explain the measured intensites. In table 5.2.1 are shown the integrated intensities of the hexagonal satellites at 10 K, which is above the ordering temperature for the magnetic moment at the cubic sites. First of all we notice that the intensities of the

satellites on each side of the (h0$\ell$) reflections, where $h \neq 0$, are not equal. Secondly, unexpected satellites appear around the (100) reflection. At present we believe that these features result from a polarization of the moments at the cubic sites. If there were no modulation of the magnetic moments, the molecular field due to the moments at the hexagonal sites should vanish at the cubic sites. The modulation of the magnetic moments gives rise to a finite component of the molecular field, which is responsible for the polarization of the moments at the cubic sites. Moon et al. (1964) suggested an improvement of the magnetic model by including a magnetic moment at the cubic sites which is 90° out of phase with that at the hexagonal sites

$$\underline{\mu}_A = \underline{\mu}_c \sin(\underline{Q}\cdot\underline{R}_{nA})$$
$$\underline{\mu}_{A'} = \underline{\mu}_c \sin(\underline{Q}\cdot\underline{R}_{nA'} + \alpha) \qquad (5.2.7)$$

In this case we get the following result for the elastic magnetic cross section:

$$\frac{d\sigma}{d\Omega} = |\hat{\kappa}x\underline{\mu}_h x\hat{\kappa}|^2 \sin^2\pi(\tfrac{h-k}{3} - \tfrac{\ell}{2}) + |\hat{\kappa}x\underline{\mu}_c x\hat{\kappa}|^2 \cos^2(\pi\tfrac{\ell}{2} + \tfrac{\alpha}{2}) + 2(\hat{\kappa}x\underline{\mu}_h x\hat{\kappa})(\hat{\kappa}x\underline{\mu}_c x\hat{\kappa}) \times \cos[\pi(h+k+\tfrac{\ell}{2}) - \tfrac{\alpha}{2}] \sin\pi(\tfrac{h-k}{3} + \tfrac{\ell}{2}) \cos(\tfrac{\pi}{2}\ell - \tfrac{\alpha}{2}) \qquad (5.2.8)$$

if $\underline{\kappa} = \underline{\tau} - \underline{Q}$, and

$$\frac{d\sigma}{d\Omega} = |\hat{\kappa}x\underline{\mu}_h x\hat{\kappa}|^2 \sin^2\pi(\tfrac{h-k}{3} - \tfrac{\ell}{2}) + |\hat{\kappa}x\underline{\mu}_c x\hat{\kappa}|^2 \cos^2(\tfrac{\pi}{2}\ell - \tfrac{\alpha}{2}) - 2(\hat{\kappa}x\underline{\mu}_h x\hat{\kappa})(\hat{\kappa}x\underline{\mu}_c x\hat{\kappa}) \times \cos[\pi(h+k+\tfrac{\ell}{2}) + \tfrac{\alpha}{2}] \sin\pi(\tfrac{h-k}{3} + \tfrac{\ell}{2}) \cos(\tfrac{\pi}{2}\ell + \tfrac{\alpha}{2}) \qquad (5.1.9)$$

if $\underline{\kappa} = \underline{\tau} + \underline{Q}$

The last term in these expressions can give rise to asymmetric contributions to the magnetic satellites. As indicated in table 5.2.2, an asymmetric contribution arises if the coupling of the moments at the cubic sites is ferromagnetic or antiferromagnetic. In both cases the model disagrees with the experimental results (see table 5.2.1).

Table 5.2.1

| h | -2 | | -1 | | 0 | | +1 | | +2 | |
|---|---|---|---|---|---|---|---|---|---|---|
| ℓ \ Q | -Q | +Q | -Q | +Q | -Q | +Q | -Q | +Q | -Q | +Q |
| 11 | | | | | | | | 10.1 | | |
| 10 | | | | | | | | 32.9 | | |
| 9 | | | | | 49.1 | 51.1 | 5.9 | 16.5 | | |
| 8 | | | | 44.2 | | | 29.6 | 19.6 | 15.7 | 24.7 |
| 7 | | | 4.9 | 14.5 | | 49.6 | 12.6 | 6.0 | 14.1 | |
| 6 | | | 49.5 | | | | 20.5 | 43.8 | 17.7 | 45.5 |
| 5 | | | 18.5 | 4.7 | | 45.2 | 3.5 | 15.2 | | 11.3 |
| 4 | | | 19.3 | 31.6 | | | 27.1 | 15.0 | 6.5 | 10.1 |
| 3 | | | 2.2 | 12.8 | 55.0 | | 11.5 | 2.3 | 9.6 | |
| 2 | | | 11.4 | 12.1 | | | 11.8 | 10.6 | 4.4 | 6.1 |
| 1 | | | 6.7 | 1.0 | 30.3 | | 1.1 | 6.5 | 2.3 | 5.6 |
| 0 | | | 2.8 | 2.4 | | | 2.2 | 2.8 | 5.3 | |

The measured integrated intensities of the magnetic satellites of Nd. ℓ and h are the Miller indices, +Q and -Q indicate the two different satellites around the nuclear reflections.

Table 5.2.2

| | | ℓ even | ℓ odd |
|---|---|---|---|
| α = 0 | h = 0 | 0 | 0 |
| | h ≠ 0 | + | 0 |
| α = π | h = 0 | 0 | + |
| | h ≠ 0 | 0 | + |

The asymmetric contribution to the (h0ℓ) reflections as it would appear if the model discussed in the text was correct. + indicates asymmetric contribution to the scattering and 0 no asymmetric contribution.

Because we only observe first-order satellites and no ferromagnetic intensity, we may write the magnetic moments in the form:

$$\underline{S}_{\ell\nu} = \underline{A}_\nu \exp(i\underline{Q}(\underline{R}_\ell + \underline{d}_\nu) + \underline{A}_\nu^* \exp(-i\underline{Q}(\underline{R}_\ell + \underline{d}_\nu)$$

where $\underline{S}_{\ell\nu}$ must be real. $\ell$ refers to the magnetic unit cell and $\nu$ to the position within this cell. The elastic magnetic cross section is found to be

$$\frac{d\sigma}{d\Omega} = \frac{N(2\pi)^3}{V} \sum_\nu \sum_{\nu'} (\hat{\kappa} \times \underline{A}_\nu \times \hat{\kappa}) \cdot (\hat{\kappa} \times \underline{A}_{\nu'}^* \times \hat{\kappa}) \times \exp(i(\underline{Q}+\underline{\kappa})(\underline{d}_\nu - \underline{d}_{\nu'})) \delta(\underline{\kappa}+\underline{Q}-\underline{\tau})$$

$$+ \frac{N(2\pi)^3}{V} \sum_\nu \sum_{\nu'} (\hat{\kappa} \times \underline{A}_{\nu'} \times \hat{\kappa}) \cdot (\hat{\kappa} \times \underline{A}_\nu^* \times \hat{\kappa}) \times \exp(i(\underline{Q}-\underline{\kappa})(d_\nu - d_{\nu'})) \delta(\underline{\kappa}-\underline{Q}-\underline{\tau}) \qquad (5.2.10)$$

If we rewrite $\underline{A}_\nu$ as

$$\underline{A}_\nu = \underline{a}_\nu + i\underline{b}_\nu \qquad (5.2.11)$$

we find

$$\frac{d\sigma}{d\Omega} = \frac{N(2\pi)^3}{V} \sum_{\nu\nu'} [\underline{a}_\nu \cdot \underline{a}_{\nu'} - (\kappa \cdot \underline{a}_\nu)(\kappa \cdot \underline{a}_{\nu'})] \exp(i\underline{\tau} \cdot (\underline{d}_\nu - \underline{d}_{\nu'}))$$

$$+ [\underline{b}_\nu \cdot \underline{b}_{\nu'} - (\hat{\kappa} \cdot \underline{b}_\nu)(\hat{\kappa} \cdot \underline{b}_{\nu'})] \exp(i\tau \cdot (\underline{d}_\nu - \underline{d}_{\nu'})) \qquad (5.2.12)$$

$$\pm i[(\underline{a}_\nu \cdot \underline{b}_{\nu'} - \underline{b} \cdot \underline{a}_{\nu'}) - ((\hat{\kappa} \cdot \underline{a}_\nu)(\hat{\kappa} \cdot \underline{b}_{\nu'}) - (\hat{\kappa} \cdot \underline{a}_{\nu'})(\hat{\kappa} \cdot \underline{b}_\nu)]$$

$$\exp i\underline{\tau} \cdot (\underline{d}_\nu - \underline{d}_{\nu'})$$

where the plus and minus signs are used for $\underline{\kappa} = \underline{\tau} \pm \underline{Q}$, respectively. Evidently the first two terms give a symmetric contribution to the magnetic satellites, while the last term gives an asymmetric contribution. If we use the notation

$$F_{\nu\nu'} = \underline{a}_\nu \cdot \underline{b}_{\nu'} - \underline{b}_\nu \cdot \underline{a}_{\nu'} - (\hat{\kappa} \cdot \underline{a}_\nu)(\hat{\kappa} \cdot \underline{b}_{\nu'}) + (\hat{\kappa} \cdot \underline{a}_{\nu'})(\hat{\kappa} \cdot \underline{b}_\nu) , \qquad (5.2.13)$$

we can write the asymmetric part of the magnetic intensity in the form

$$I_{asym} = const \cdot i \cdot \sum_{\nu\nu'} F_{\nu\nu'} \exp(i\underline{\tau}\cdot(\underline{d}_\nu - \underline{d}_{\nu'})$$
$$= C \sum_{\nu>\nu'} F_{\nu\nu'} \sin\underline{\tau}\cdot(\underline{d}_\nu - \underline{d}_{\nu'}). \qquad (5.2.14)$$

The problem now is to choose the $a_\nu$ and $b_\nu$ in such a way that the following conditions are satisfied:

the c-axis is a symmetry axis.
$I_{asym}$ changes sign going from (1,0,1) to (1,0,3).

The problem can only be solved by using a least squares fit to the intensities found experimentally. The problem in doing this is, of course, the large number of parameters (in general 24). A program has been set up, but the procedure has not yet been carried through successfully, because the problem of putting the right constraints into the model still remains. We must, therefore, conclude that the magnetic structure of Nd is very complicated, and we have not yet been able to find the right structure.

## 5.3. Critical behaviour of Nd

The mean field theory gives the following result for the spontaneous magnetization as a function of the temperature

$$\frac{M}{M_o} = B_J\left(\frac{3J}{J+1}\frac{T_c}{T}\frac{M}{M_o}\right)$$

where $M_o$ is the saturation magnetization. If we expand the Brillouin function $B_J$ around the critical temperature $T_c$, we get the following result

$$\frac{M}{M_o} \simeq \frac{T_c}{T}\frac{M}{M_o} - \frac{(2J^2+2J+1)^3}{10J(J+1)^2}\left(\frac{T_c}{T}\right)^3\left(\frac{M}{M_o}\right)^3 \qquad (5.3.1)$$

$$\left(\frac{M}{M_o}\right)^2 \simeq \frac{10J(J+1)^2}{3(2J^2+2J+1)}\left(\frac{T}{T_c}\right)^2\left(1-\frac{T}{T_c}\right) \qquad (5.3.2)$$

$$\left(\frac{M}{M_o}\right) \approx \left(\frac{10J(J+1)^2}{3(2J^2+2J+1)}\right)^{\frac{1}{2}} \left(\frac{T_c-T}{T_c}\right)^{\frac{1}{2}} \qquad (5.3.3)$$

and an interesting fact emerges. The spontaneous magnetization always obeys the same power law as a function of temperature. The power (the critical exponent) is independent of the magnetic material and has the universal value:

$$\beta = 1/2. \qquad (5.3.4)$$

According to the Landau theory (1968), this universality is even more general. The Landau theory of critical phenomena states that the critical exponent for any order parameter is ½. Evidently, the Landau theory is too simplified because the experimentally found values differ from those predicted by the theory, although there seems to be some similarity between the critical exponents of systems with the same dimensionality. The reason why the Landau theory predicts an incorrect exponent is that it includes no fluctuations. Fluctuations in the order parameter are, of course, very important at the critical point. In fact, the Landau theory is internally inconsistent because it predicts that the correlation length goes to infinity near the transition temperature. Hence, near the transition temperature, the fluctuations in the system must be taken seriously. Wilson (1974) overcame this difficulty and suggested a new approach to critical phenomena. This theory is normally referred to as renormalization group theory. It predicts that the Landau theory is correct in 4 dimensions, but it only gives exact results in 3 dimensions in very few cases. Normally, the results must be expanded in $\varepsilon = 4-d$, where d is the dimension. For example, for an Ising system, Wilson et al. (1974) found that

$$\beta \approx \frac{1}{2} - \frac{\varepsilon}{6}, \qquad (5.3.5)$$

or $\beta \approx 1/3$ in 3 dimensions in good agreement with the experiments. Based on symmetry arguments, Mukamel et al. (1976) were able to divide second-order phase transitions into groups, and by use of renormalization group theory and the $\varepsilon$-expansion they calculated the critical exponents for each group. Their

result for the group to which Nd belongs, if it has the magnetic structure proposed by Moon et al. (1964), is

$$\beta = 0.38. \qquad (5.3.6)$$

As discussed in the previous section, the magnetic structure of Nd differs from this model. Hence it is not surprising that, for Nd, the critical exponent derived from neutron diffraction differs from that calculated by Mukamel et al., but it is surprising that we get a result that is close to the classical result ½ (see fig. 5.3.1). A least squares fitting to the

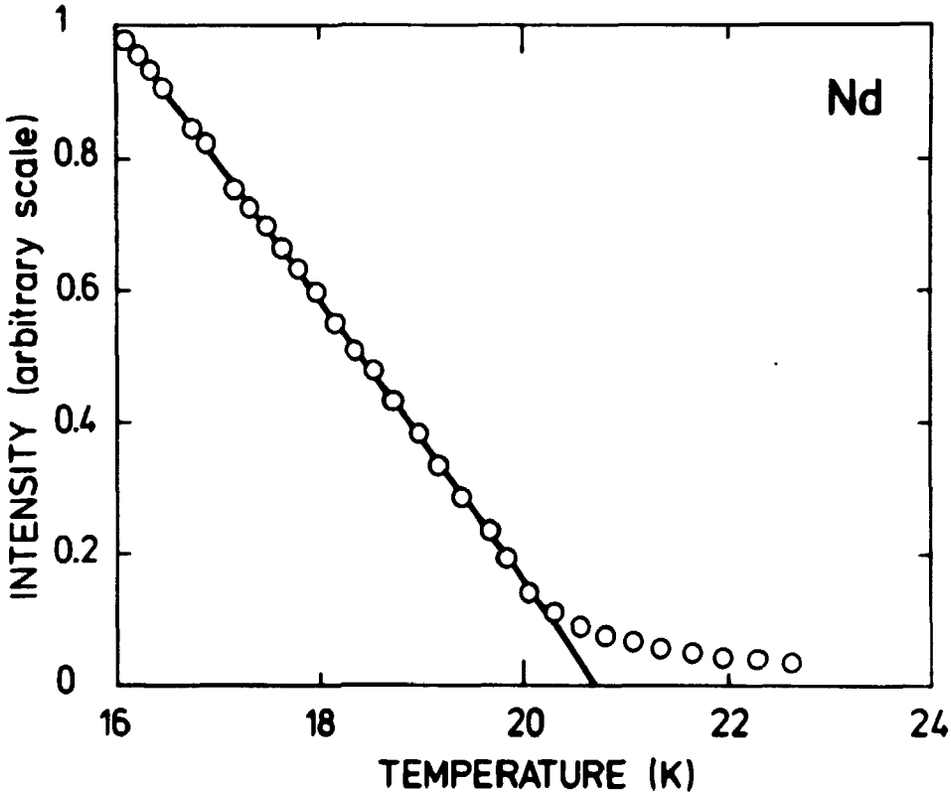


Fig. 5.3.1. The intensity of the (Q,0,3) satellite as function of temperature. The straight line gives the critical exponent ½. The long tail of scattering above the Néel temperature (20.71K) is probably due to a smearing effect of the transition temperature.

experimental points shows that

$$\beta = 0.48 \pm 0.02 \qquad (5.3.7)$$

and

$$T_c = 20.71 \pm 0.05 \text{ K} \qquad (5.3.8)$$

Before the magnetic structure of Nd has been solved, it is not possible to state why the exponent has this value. Renormalization group theory can lead to the result ½. This is the case for a dipolar-coupled Ising antiferromagnet, and this has been verified by measurements on $LiTbF_4$ by Als-Nielsen et al. (1974).

As seen in fig. 5.3.1, there is a long tail of finite scattering above the critical temperature. Some of this scattering results from critical scattering, but the tail is too long to be fully explained by this effect. We believe that it is caused by a smearing of the transition temperature. This smearing effect is caused by the fact that even in a pure element the transition temperature is not a definite temperature,but a small interval of temperatures.

Note added in proof: A reanalysis (Lebech to be published 1978) of the elastic neutron scattering data presented in fig. 5.3.1 shows that by correcting properly for the critical scattering below $T_N = 19.9$ K; $\beta = 0.37$ in accordance with $\beta$-value expected from $\varepsilon$-expansion and renormalization group theory.

# 6. MAGNETIC STRUCTURE OF MnSi

## 6.1. Introduction

The nuclear structure of MnSi is cubic but rather complex. The structure belongs to the space group $T^4$-$P2_13$ with four Mn atoms in the positions $(x,x,x)$, $(x+\frac{1}{2}, \frac{1}{2}-x, \bar{x})$, $(\bar{x},x+\frac{1}{2},\frac{1}{2}-x)$ and $(\frac{1}{2}-x,\bar{x},x+\frac{1}{2})$ and four Si atoms in similar positions with (Pauling and Soldate 1948)

$$x_{Mn} = 0.137 \quad \text{and} \quad x_{Si} = 0.842.$$

The dimension of the unit cell is given by

$$a = 4.489 \text{ Å}.$$

Previous measurements of the magnetic behaviour of MnSi have given rather confusing results. Shinoda and Asanabe measured the susceptibility and found that MnSi is ferromagnetic below 38 K with a saturation moment of 0.3 $\mu_B$ per Mn atom. This should be compared to the paramagnetic moment of 2.0 $\mu_B$ obtained from the Curie constant. In fig. 6.1.1 we show the magnetization curve with the field in the (111) direction. The crystal was first made multidomain by cooling from 45 K in zero field. As seen, the magnetization curve is remarkably linear up to a well defined critical field of 5.85 kGauss. This suggests that MnSi is not a simple ferromagnet, although it behaves as a ferromagnet above the critical field. In fig. 6.1.2 is shown the magnetization curves with the field in the (110) and the (001) directions, respectively. As seen, there is a small deviation from linear behaviour. This behaviour was interpreted by Levinson et al. (1972) as a spin-flop transition. These authors suggested that MnSi is antiferromagnetic at low fields and has a spin-flopped phase between 1.5 kGauss and 6 kGauss, and that it is ferromagnetically ordered above 6 kGauss. In the antiferromagnetic phase, Levinson et al.(1972) suggested that MnSi is not an antiferromagnet in the normal sense, because a neutron diffraction experiment showed no evidence of antiferromagnetic ordering. On the contrary, they found that MnSi is ferromagnetic. Unfortunately, the ratio of the magnetic to nuclear intensity is such that one would only expect to find detectable magnetic

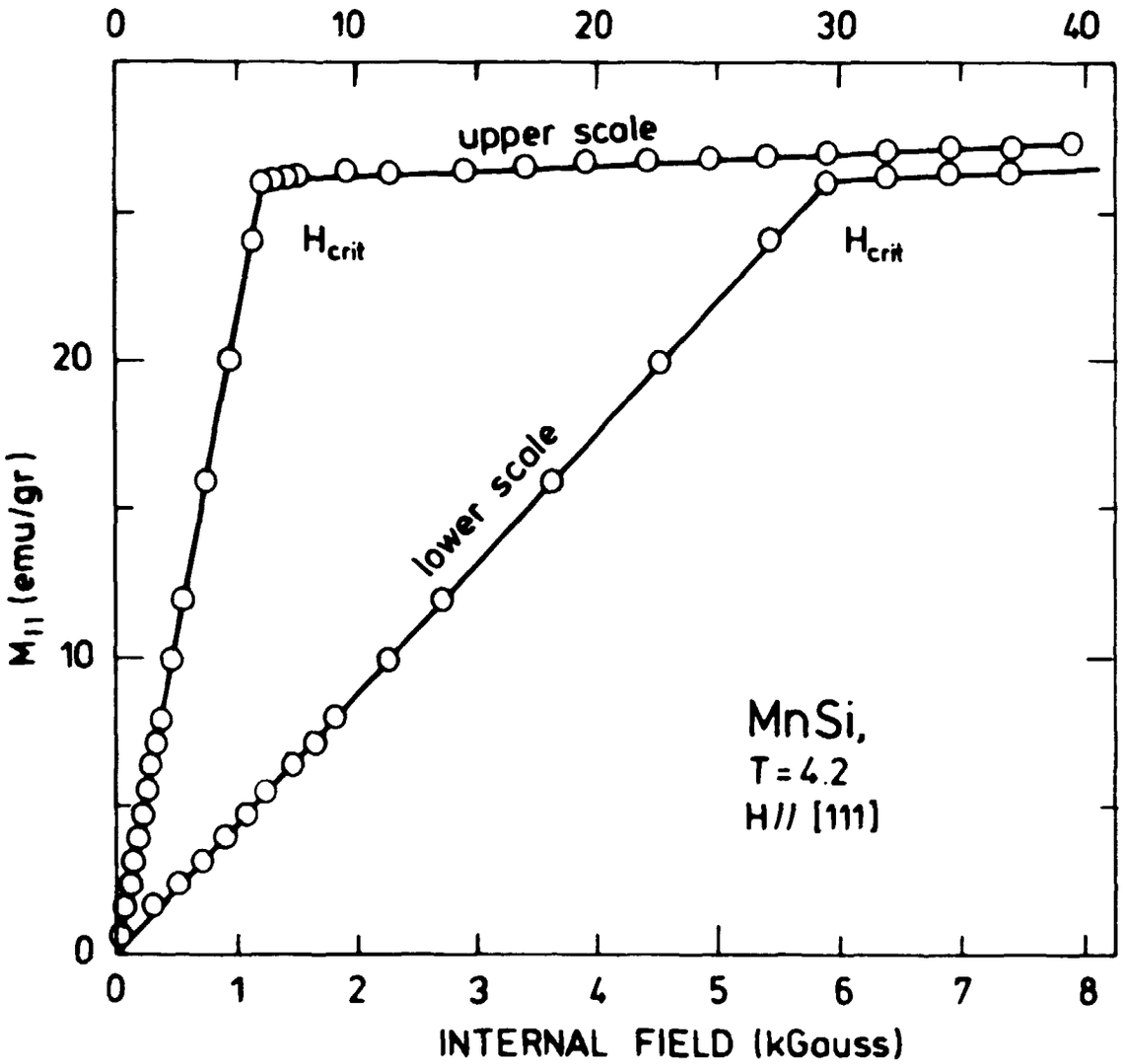


Fig. 6.1.1. Magnetization curve of MnSi (upper scale). The lower scale has been expanded to show the linearity in the low field region.

scattering in the (210) reflection, and Levinson et al. (1972) concluded that MnSi is ferromagnetic, but the magnetic domains are antiferromagnetically ordered. By measuring the depolarization factor for polarized neutrons transmitted through a thin MnSi sample, they were able to deduce that the size of each ferromagnetic domain is $\sim$ 500 Å. Our aim in doing neutron diffraction experiments on MnSi was to test this model and look for phase transitions by applying a magnetic field. As we shall see below, a very different model of the magnetic structure resulted from our measurements (Hansen et al. 1976).

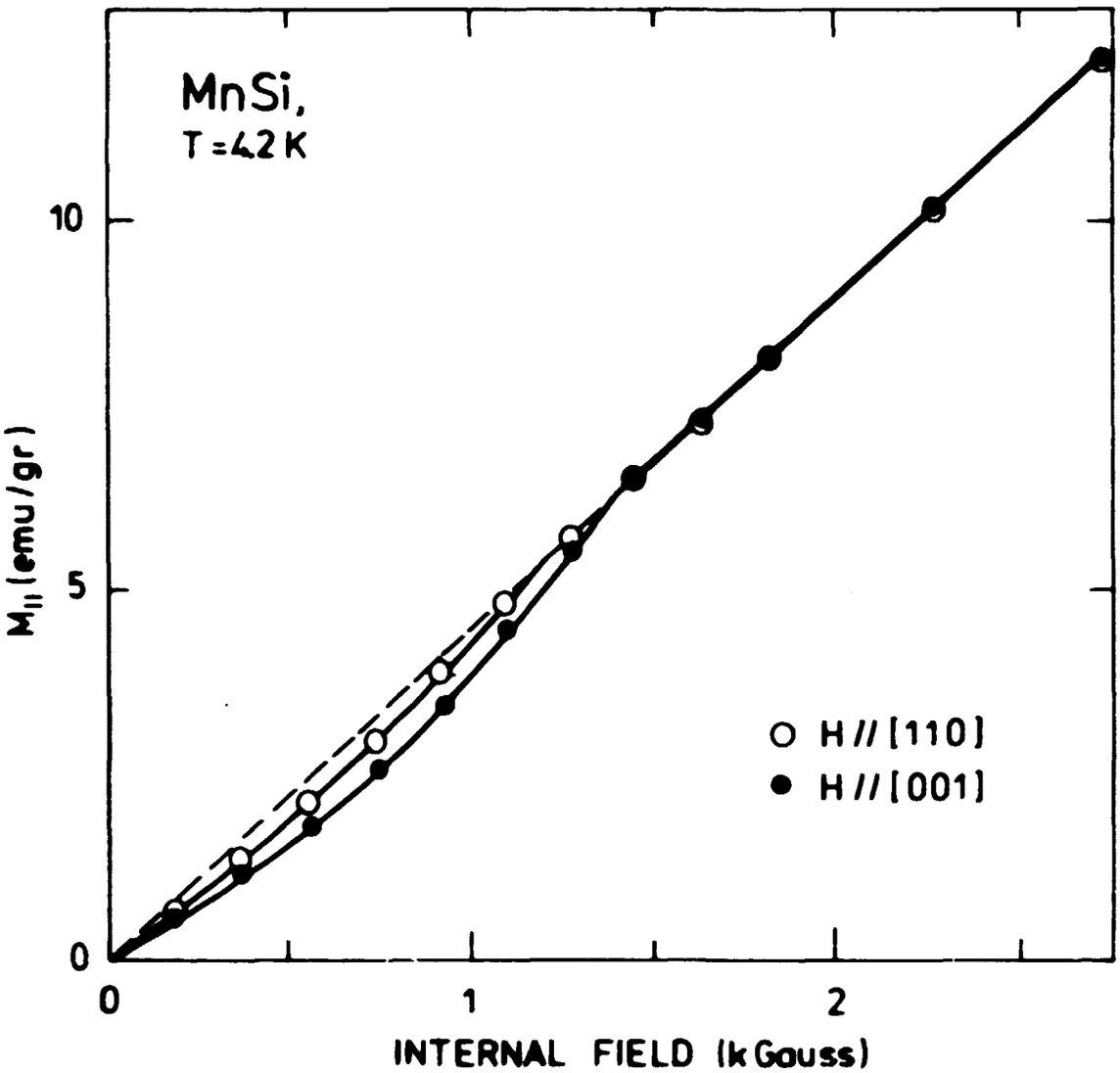


Fig. 6.1.2. Magnetization curve of MnSi. The small deviation from linear behaviour has been interpreted as a spin-flop transition, but is due to the helix structure of MnSi.

## 6.2. Experimental results

For neutron diffraction purposes, a thin plate, of dimensions 30 x 3 x 0.5 mm, was cut from a large single crystal of MnSi by means of a spark cutter. A small sphere, of 5 mm diameter, was cut from the same crystal and used for the magnetization experiment. In order to repeat the neutron diffraction experiment of Levinson et al. (1972), we measured the intensity of the (021) reflection for temperatures between 4.2 and 40 K. Figure 6.2.1 shows the difference patterns between scans at 9 and 35 K obtained with a magnetic field applied in the (100) direction. The absence of scattering in zero field at 0 $A^{-1}$ (021) shows

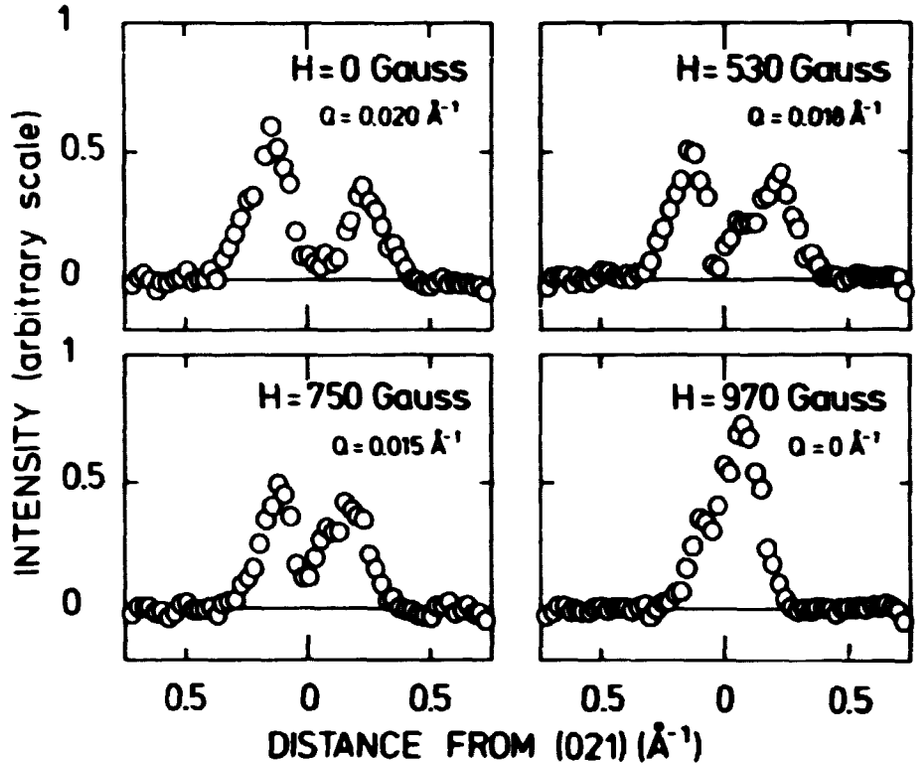


Fig. 6.2.1. Difference pattern of the scans through the (021) reflection at 9 K and 35 K obtained with a magnetic field in the (100) direction which is perpendicular to the scattering plane. The magnetic satellites show that the magnetic structure is a helix structure. The transition at 1 kGauss is probably into a cone structure with the cone axis along the 100-direction. The satellites then lie along an axis perpendicular to the scattering plane and cannot be seen.

that there is no ferromagnetic intensity. The figure, however, clearly shows the existence of two magnetic satellites. We therefore conclude that MnSi has a helix structure. The scan was a rock scan through the (021) reflection, but the modulation vector is not necessarily perpendicular to the reciprocal lattice vector of the (021) reflection. In order to find the direction and size of the modulation vector, we had to reorientate the sample and obtain a much better resolution. Therefore, the sample was mounted on a triple-axis spectrometer located at the cold neutron source at DR 3. The intensity of neutrons with small energies is much higher from the cold source than from the normal thermal beam. Hence, we obtained a better resolution without losing the intensity, and could measure the satellites around (000) and (011). These measurements showed that the modulation vector is in the (111) direction and of the size $0.036\ Å^{-1}$. This corresponds to a turn-angle of $3.27^{o}$ per layer and a repetition length of 175 Å. Because of this long wave-

length of the modulated structure, it is almost ferromagnetic. This may explain the contradicting results of the previous experiments.

As the field is increased, the satellites seem to disappear at approximately 1 kGauss, and increased intensity is observed at (021). According to Ishikawa et al. (1976), the structure is still a helix structure with the modulation vector in the field direction. This does not disagree with our results, as we measured in a plane perpendicular to the magnetic field and satellites in the field direction would show up as intensity at (021) because of insufficient vertical resolution. Therefore, we believe that the magnetic structure is a cone structure with the cone axis parallel to the magnetic field for fields higher than 1 kGauss. For fields lower than the 1 kGauss, it is reasonable to believe that the structure is a spiral structure with the moments perpendicular to the screw axis (the (111) direction). The intensities of the (021) reflection and the

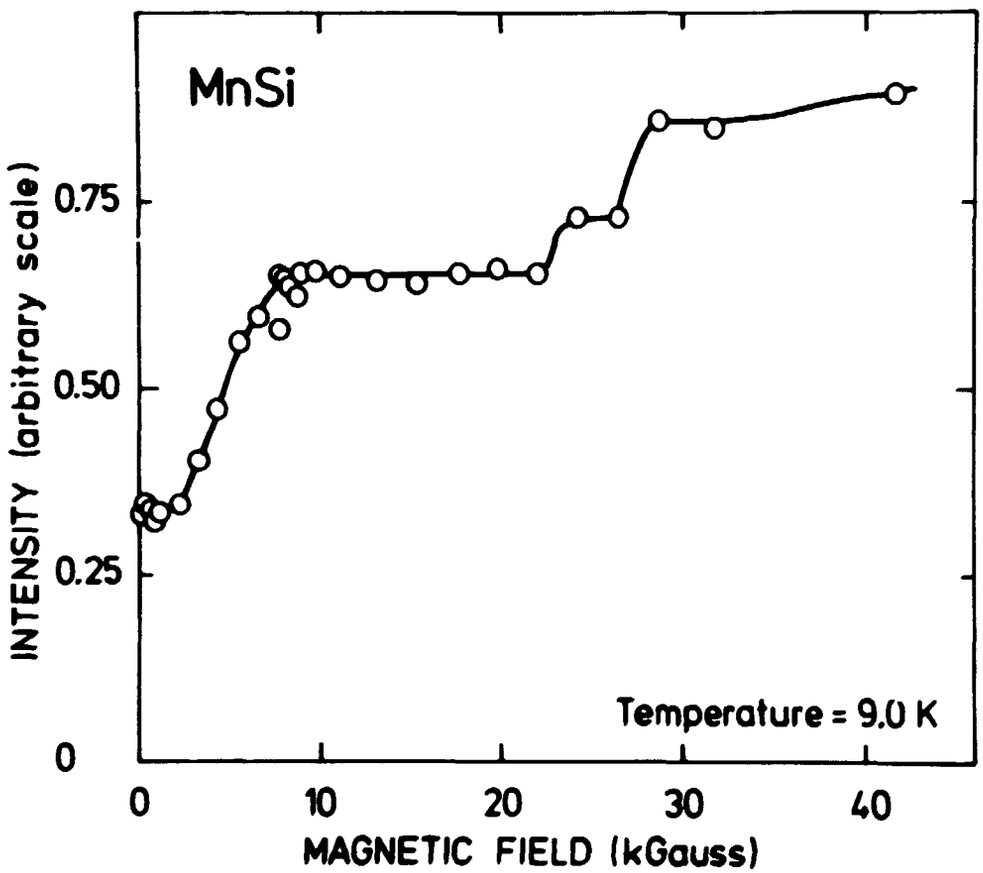


Fig. 6.2.2. The magnetic intensity of the (021) reflection as function of the magnetic field. The nuclear intensity has been subtracted by subtraction of a similar scan above the transition temperature. As seen, there are phase transions at 6, 22 and 28 kGauss.

satellites around this reflection were measured by performing rock scans through the (021) reflection. In order to find the magnetic intensity, the high temperature integrated intensity of a similar scan was subtracted. The results are shown in fig. 6.2.2 as a function of the magnetic field. The linear increase between 1 and 6 kGauss indicates that the cone closes up in this region. Above 6 kGauss, the sample is ferromagnetic, but there are transitions at 22 and 28 kGauss which should be further investigated. The temperature dependence of the magnetic intensity is shown in fig. 6.2.3 in a zero magnetic field and in a field of 10.8 kGauss. We were able to measure the

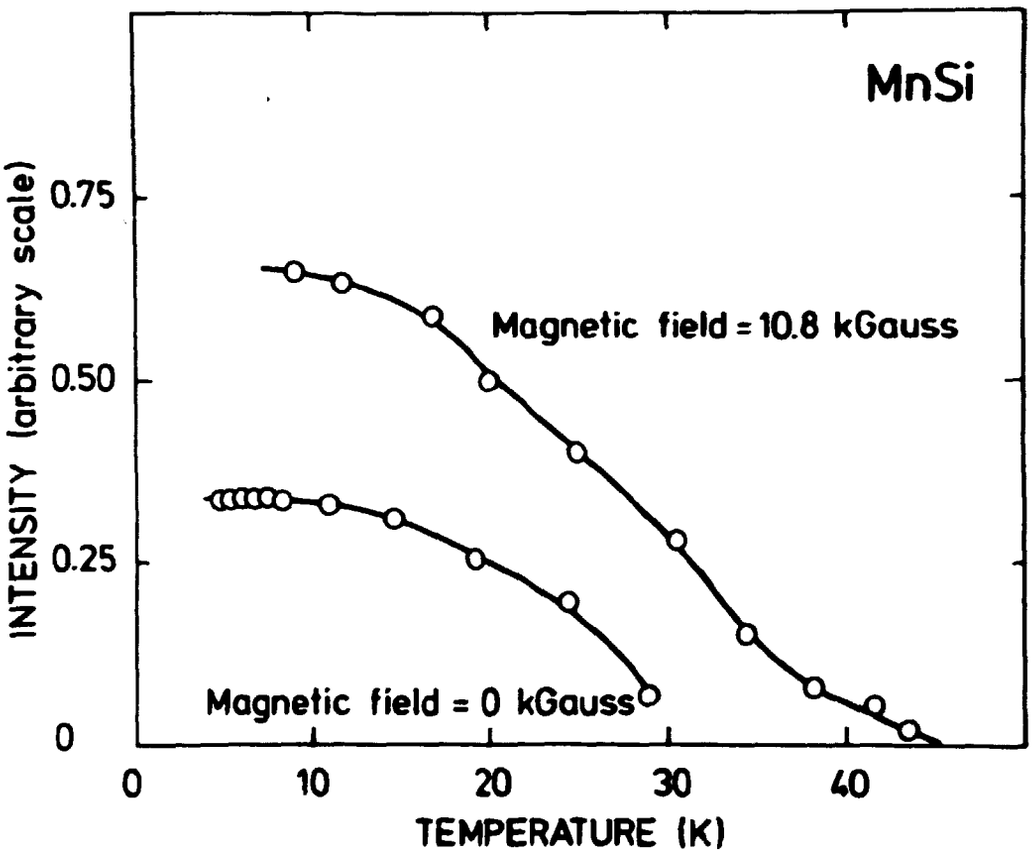


Fig. 6.2.3. The magnetic intensity at the (021) reflection in zero magnetic field and in a field of 10.8 kGauss as function of temperature.

intensity of the satellites around (100) and (011) using the triple-axis spectrometer. The temperature dependence of the integrated intensity of these satellites is shown in fig. 6.2.4. The ratio of the intensity of the $(\bar{Q},Q,Q)$ satellite to the $(\bar{Q}, 1+Q, 1+Q)$ satellite is very large indicating a sharp rise in the magnetic form factor in the forward direction. Hence, the magnetic moment is widely spread out in real space. This observation, together with the long wavelength of the helix

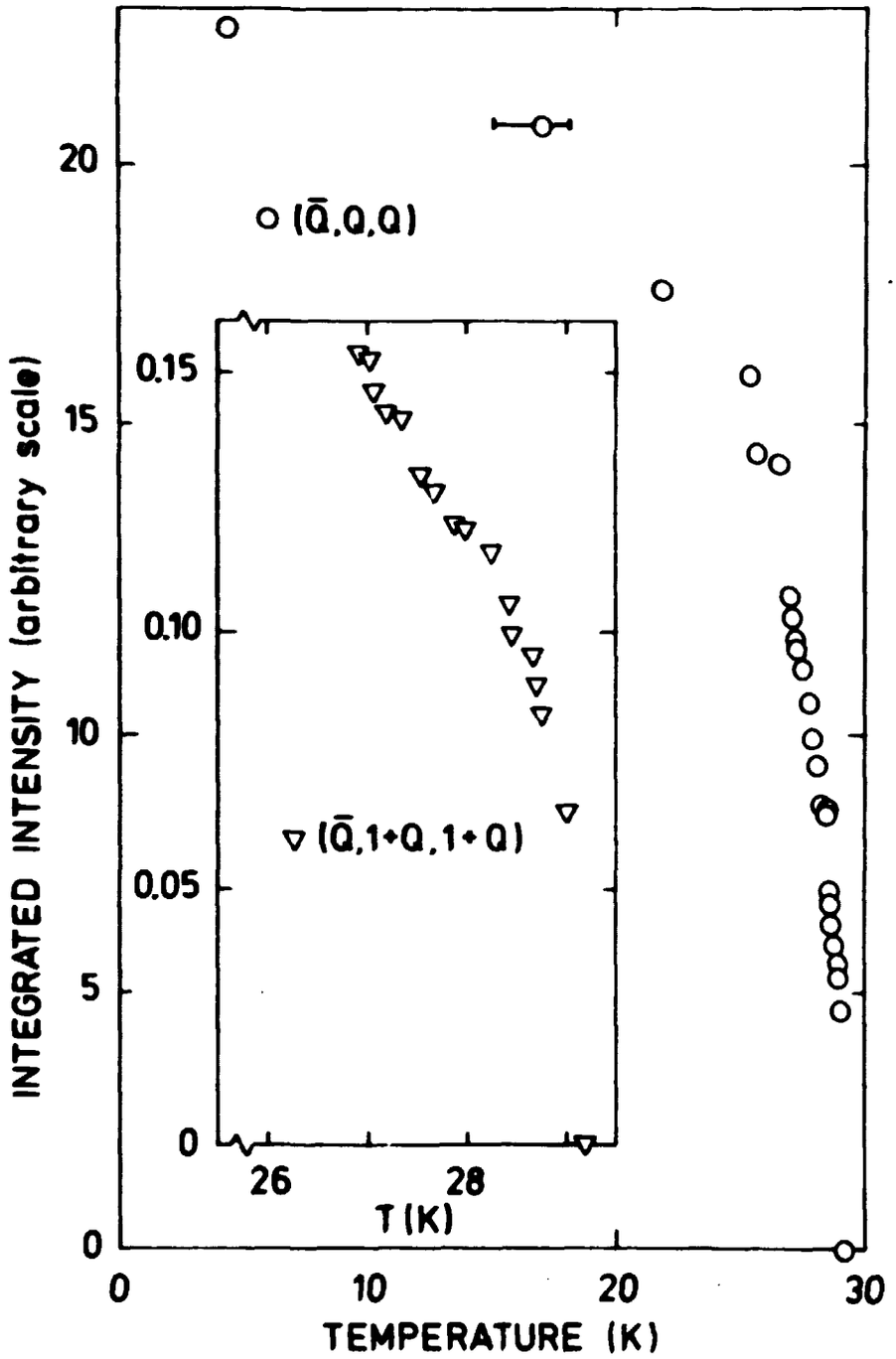


Fig. 6.2.4. The intensity of the $(\bar{Q},Q,Q)$ satellites as function of temperature near the transition temperature. The sharp rise in the intensity indicates a first-order transition.

structure, indicates that the magnetic moment originates from nearly itinerant electrons.

The transition from ordered to disordered phase at 28.7 K is very sharp. A least squares fit to the power law

$$\frac{M}{M_o} = \left(\frac{T-T_c}{T_c}\right)^{\beta}$$

gives a value of less than 0.2 for the critical exponent $\beta$. This suggests that the transition could be of first order. The magnetization measurements also indicate a first-order transition. Unfortunately, the value of $\beta$ obtained from the $(\bar{Q}, 1+Q, 1+Q)$ satellite differed from that obtained from the $(\bar{Q}, Q, Q)$ satellite. Further investigations of the transition are therefore required.

## 6.3. Conclusions

The investigation of MnSi was only preliminary. In contrast to the previous experiments on MnSi, we were able to deduce that the magnetic structure is a helix structure with a very long periodicity. In zero field the structure is presumably a spiral structure with the moments perpendicular to the screw axis,which is the (111) direction. At higher fields, the structure transforms to a cone structure and above 6.0 kGauss it is ferromagnetic. The magnetic moment seems to be widely spread out in direct space indicating that it originates from purely itinerant electrons. This last point makes MnSi very attractive for further investigations because the results can be compared with band calculations. It is also interesting to notice that the transition from an ordered to a disordered phase seems to be of first order.

ACKNOWLEDGEMENT

I wish to thank my supervisor B. Lebech for her great help during this project. I also wish to thank G.B. Jensen and P.B. Fynbo for many valuable discussions and their help during the preparation of the samples.

REFERENCES

ALS-NIELSEN, J., HOLMES, L.M., and GUGGENHEIM, H.J. (1974) Phys. Rev. Lett. 32, 610-613.

BOZORTH, R.M.(1967) J. Appl. Phys. 38, 1366-1371.

BRUN, T.O. and LANDER, G.H. (1969) Phys. Rev. Lett. 23, 1295-1298.

BRUN, T.O., FELCHER, G.P., and LANDER, G.H. (1971) J. Phys. (Paris) 32, C1/577-C1/578.

COOPER, B.R. (1972). In: Magnetic properties of rare earth metals. Edited by R.J. Elliott (Plenum, London) 17-80.

DIETRICH, O.W. and ALS-NIELSEN, J. (1967) Phys. Rev. 162, 315-320.

FREEMAN, A.J. and WATSON, R.E. (1962) Phys. Rev. 127, 2058-2075.

HANSEN, P. and LEBECH, B. (1976). J. Phys. F: Metal Phys 6, 2179-2189.

HANSEN, P.Å., NIELSEN, O.V., and STORGÅRD, F. Magnetic anisotropy and phase transitions in antiferromagnetic MnSi. International Conf. on Magnetism, Amsterdam, The Netherlands, September 6-10, 1976.

HOUMANN, J.G., JENSEN, J., and TOUBORG, P. (1975) Phys. Rev. B12, 332-344.

ISHIKAWA, Y., TAJUMA, K., BLOCH, D., and ROTH, M. (1976) Solid State Commun. 19, 525-528.

JENSEN, J., HOUMANN, J.G., and BJERRUM MØLLER, H. (1975a) Phys. Rev. B12, 303-319.

JENSEN, J. and HOUMANN, J.G. (1975b) ibid. 320.

KAPLAN, T.A. (1961) Phys. Rev. 124, 329-339.

KAPLAN, T.A. and LYONS, P.M. (1963) Phys. Rev. 129, 2072-2087.

KASUYA, T. (1965) Prog. Theor. Phys. 16, 45-57.

KASUYA, T. (1966). In: Magnetism. Edited by G.T. Rado and H. Suhl. Vol. 2B. (Academic Press, New York) 215-294.

KOEHLER, W.C., CABLE, J.W., WOLLAN, E.O., and WILKINSON, M.N. (1962) Phys. Rev. 126, 1672-1679.

KOEHLER, W.C., CABLE, J.W., CHILD, H.R., and WILKINSON, M.N.. (1963) J. Appl. Phys. Suppl. 34, 1335-1336.

KOEHLER, W.C. (1972). In: Magnetic properties of rare earth metals. Edited by R.J. Elliott (Plenum, London) 81-128.

LANDAU, L.D. and LIFSHITZ, E.M. (1968) Statistical physics. 2.ed. (Pergamon, Oxford) 424-454.

LANDER, G.H., BRUN, T.O., and VOGT, O. (1973) Phys. Rev. B7, 1988-2004.

LEBECH, B. and NIELSEN, M. (1975). In: New methods and techniques in neutron diffraction. Proceedings of the neutron diffraction conference, Petten, August 5-6 1975 (Petten) (RCN-234) 466-486.

LEBECH, B. and HANSEN, P.Å. (1977). Fourth European Crystallographic Meeting, Oxford, U.K. August 30 - September 3, 1977, PI.76.

LEVINSON, L.M., LANDER, G.H., and STEINERTZ, M.O. (1973) AIP Conf. Proc. 10, 1138-1142.

LINDGAARD, P.-A.(1976a) AIP Conf. Proc. 29, 441-442.

LINDGAARD, P.-A.(1976b) Phys. Rev. B14, 4074-4086.

MARSHALL, W. and LOVESEY, S.W., Theory of thermal neutron scattering (Clarendon, Oxford) 599 pp.

McEWEN, K.A. and TOUBORG, P. (1973) J. Phys. F3, 1903-1909.

MILLHOUSE, A.H. and KOEHLER, W.C. (1971) Int. J. Magnet. 2, 389-403.

MOON, R.M., CABLE, J.W., and KOEHLER, W.C. (1964) J. Appl. Phys. 35, 1041-1042.

MUKAMEL, D., KRINSKY, A., and BAK, P. (1975) AIP Conf. Proc. 29, 474-479.

NAGAMIYA, T. (1967) Solid State Phys. 20, 305-411.

NIGH, M.E. (1963) J. Appl. Phys. 34, 3323-3324.

PAULING, L. and SOLDATE, A.M. (1948) Acta Crystallogr. 1, 212-216.

ROTH, L.M., ZEIGER, H.J., and KAPLAN, T.A. (1966) Phys. Rev. 149, 519-525.

RUDERMAN, M.A. and KITTEL, C. (1954) Phys. Rev. 96, 99-102.

SHINODA, D. and ASANABE, S. (1966) J. Phys. Soc. Japan 21, 555.

SHIRANE, G. and PICKART, J. (1966) J. Appl. Phys. 37, 1032-1033.

SLICHTER, C.P. (1963) Principles of magnetic resonance with examples from solid state physics (Harper and Row, New York) 164.

SPEDDING, F.H., ITO, Y., and JORDAN, R.G. (1970) J. Chem. Phys. 53, 1455-1465.

STEVENS, K.W.H. (1952) Proc. Phys. Soc. A65, 209-215.

TOUBORG, P. (1977) to be published.

TOUBORG, P. (1970), Magnetiske egenskaber af europium og holmium-terbium legeringer. Lic. tech. dissertation (DTH, Lyngby) 164 pp.

WILSON, K.G. and KOGUT, J. (1974) Phys. Rept. 12C, 75-200.

YOSIDA, K. (1957) Phys. Rev. 106, 893-898.